

Single-cell transcriptomic profiling of the aging mouse brain

Methodios Ximerakis^{1,2,3,8*}, Scott L. Lipnick^{1,2,3,4,8}, Brendan T. Innes⁵, Sean K. Simmons³, Xian Adiconis³, Danielle Dionne³, Brittany A. Mayweather^{1,2}, Lan Nguyen³, Zachary Niziolek⁶, Ceren Ozek^{1,2}, Vincent L. Butty⁷, Ruth Isserlin⁵, Sean M. Buchanan^{1,2}, Stuart S. Levine⁷, Aviv Regev³, Gary D. Bader⁵, Joshua Z. Levin³ and Lee L. Rubin^{1,2,3*}

The mammalian brain is complex, with multiple cell types performing a variety of diverse functions, but exactly how each cell type is affected in aging remains largely unknown. Here we performed a single-cell transcriptomic analysis of young and old mouse brains. We provide comprehensive datasets of aging-related genes, pathways and ligand–receptor interactions in nearly all brain cell types. Our analysis identified gene signatures that vary in a coordinated manner across cell types and gene sets that are regulated in a cell-type specific manner, even at times in opposite directions. These data reveal that aging, rather than inducing a universal program, drives a distinct transcriptional course in each cell population, and they highlight key molecular processes, including ribosome biogenesis, underlying brain aging. Overall, these large-scale datasets (accessible online at https://portals.broadinstitute.org/single_cell/study/aging-mouse-brain) provide a resource for the neuroscience community that will facilitate additional discoveries directed towards understanding and modifying the aging process.

Aging, the time-dependent functional decline of organs and tissues, is the biggest risk factor for many diseases, including several neurodegenerative and cardiovascular disorders¹. Characterizing aging-related molecular and cellular changes will provide insights into this complex process and highlight opportunities to slow or reverse its progression, thereby helping to prevent or treat aging-associated pathologies. That this might be achievable is supported by a plethora of studies using model organisms, demonstrating that not only lifespan but also the integrity of multiple tissues can be regulated by discrete molecular modifications^{2,3}.

Towards the goal of achieving a broader understanding of aging-related changes and deciphering the molecular mechanisms that accompany brain aging, transcriptomic studies in model organisms and humans have been at the forefront of experiments. However, these studies generally use aggregated RNA from either mixed cell populations^{4–6}, which may vary in distinct ways with age, or from cell populations purified using known markers^{7–9}, which themselves may also change during aging. Therefore, despite the successful identification of major aging-related genes and pathways, previous transcriptomic analyses have not resolved the common aging-related changes experienced across all brain cells from those that may be cell-type specific. Thus, there is a need to elucidate how individual cell types are affected by aging and to clarify if the process of aging follows a similar blueprint in all cell types or whether certain cell types have unique transcriptional changes. This information will be critical in determining whether aging at the tissue level is a global process, if it results from specific changes in certain cell populations that culminate in loss of function and deterioration, or a combination of both¹⁰. This information may also help the design of effective aging-related therapeutics that are targeted

either narrowly, affecting only certain cell types, or more broadly, affecting all cells.

In this study, to begin to address these issues, we used single-cell RNA sequencing to profile and compare the cellular composition and transcriptomes of young and old mouse brains. For all the major cell populations, we provide comprehensive datasets of genes and pathways whose transcriptional profiles change with aging. Our computational analysis suggests that cells in the brain do not change with aging identically, indicating that, while overlapping signatures exist, the cellular consequences of aging are not universal. Given that cell nonautonomous changes are also known to regulate aging-dependent changes², we also detail ligand–receptor interactions among nearly all the cell types in the brain that are modified by aging. Overall, this study provides a rich resource that can facilitate the interrogation of the molecular underpinnings and cellular basis of the aging process in the mouse brain.

Results

Identification of cell types. To gain new, more precise, insights into the effects of aging, we used unbiased high-throughput single-cell RNA sequencing (scRNA-seq) to examine the transcriptional profiles of young and old mouse brains (Fig. 1a). Because the dissociation of mammalian adult brains is challenging due to the complexity of the tissue, we first developed a new dissociation protocol that enables the isolation of healthy and intact cell suspensions that are representative of both young and old brains (see details in Methods).

We then analyzed the transcriptomes of 50,212 single cells (24,401 young and 25,811 old) derived from the brains of 8 young (2–3 months) and 8 old (21–23 months) mice (Supplementary Fig. 1–2). We first aggregated transcriptionally similar cells, using

¹Department of Stem Cell and Regenerative Biology, Harvard University, Cambridge, MA, USA. ²Harvard Stem Cell Institute, Cambridge, MA, USA. ³Broad Institute of Massachusetts Institute of Technology and Harvard, Cambridge, MA, USA. ⁴Department of Biomedical Informatics, Harvard Medical School, Boston, MA, USA. ⁵The Donnelly Centre, University of Toronto, Toronto, ON, Canada. ⁶Bauer Core, Faculty of Arts and Sciences Division of Science, Harvard University, Cambridge, MA, USA. ⁷BioMicro Center, Massachusetts Institute of Technology, Cambridge, MA, USA. ⁸These authors contributed equally: Methodios Ximerakis, Scott L. Lipnick. *e-mail: methodios_ximerakis@harvard.edu; lee_rubin@harvard.edu

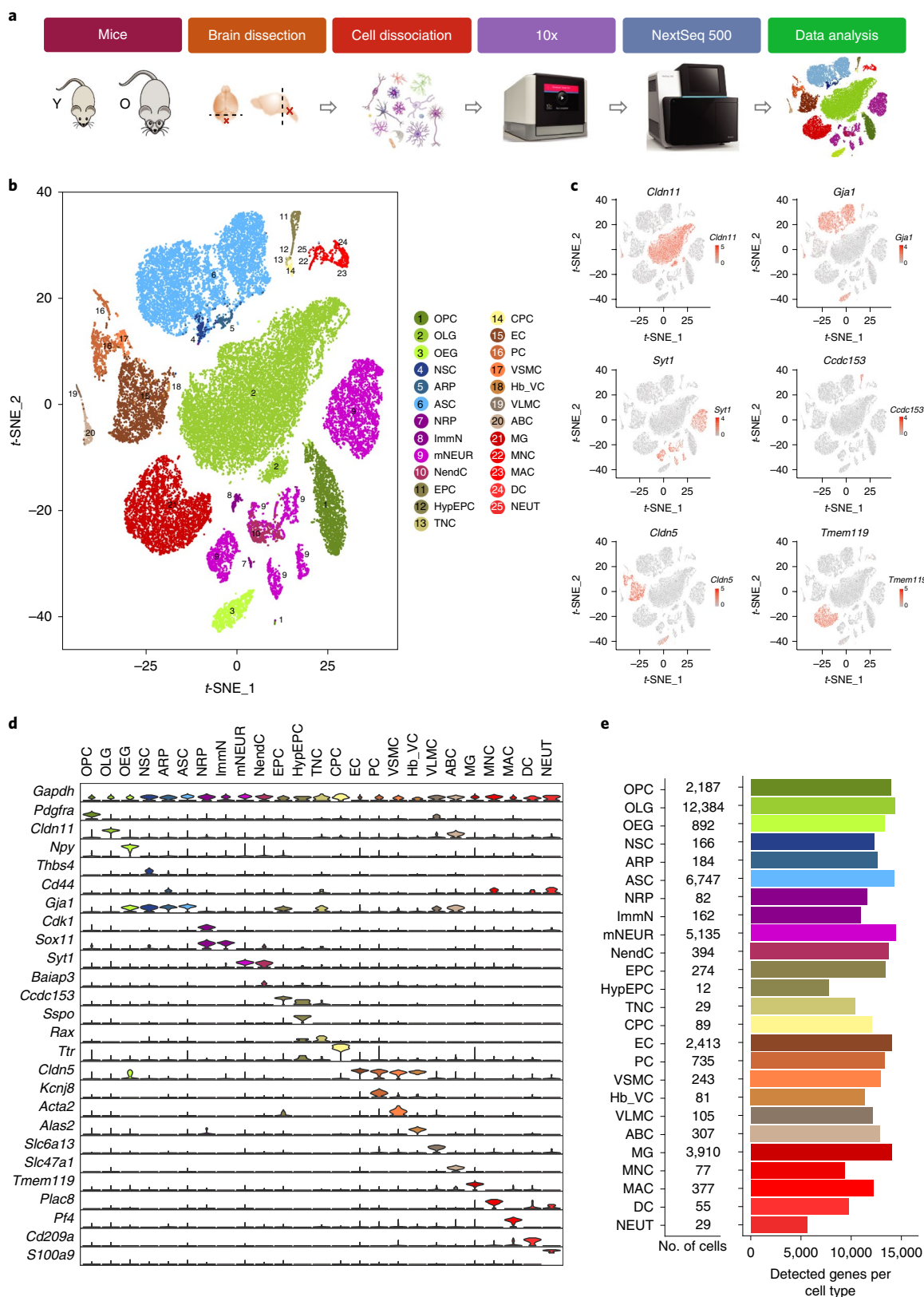


Fig. 1 | Identification of cell types. **a**, Overview of the experimental workflow. **b**, *t*-Distributed stochastic neighbor embedding projection of 37,069 single-cell transcriptomes (16,028 from 8 young mouse brains and 21,041 from 8 old mouse brains). Cell clusters were color coded and annotated post hoc based on their transcriptional profile identities (see details in Methods). **c**, *t*-Distributed stochastic neighbor embedding visualization of 6 major cell populations showing the expression of representative well-known cell-type-specific marker genes. Numbers reflect the number of UMI detected for the specified gene for each cell. **d**, Violin plot showing the distribution of expression levels of well-known representative cell-type-enriched marker genes across all 25 cell types ($n=37,069$ cells) (see details in Methods). **e**, Bar plot showing the total number of detected cells and the total number of detected genes per cell type.

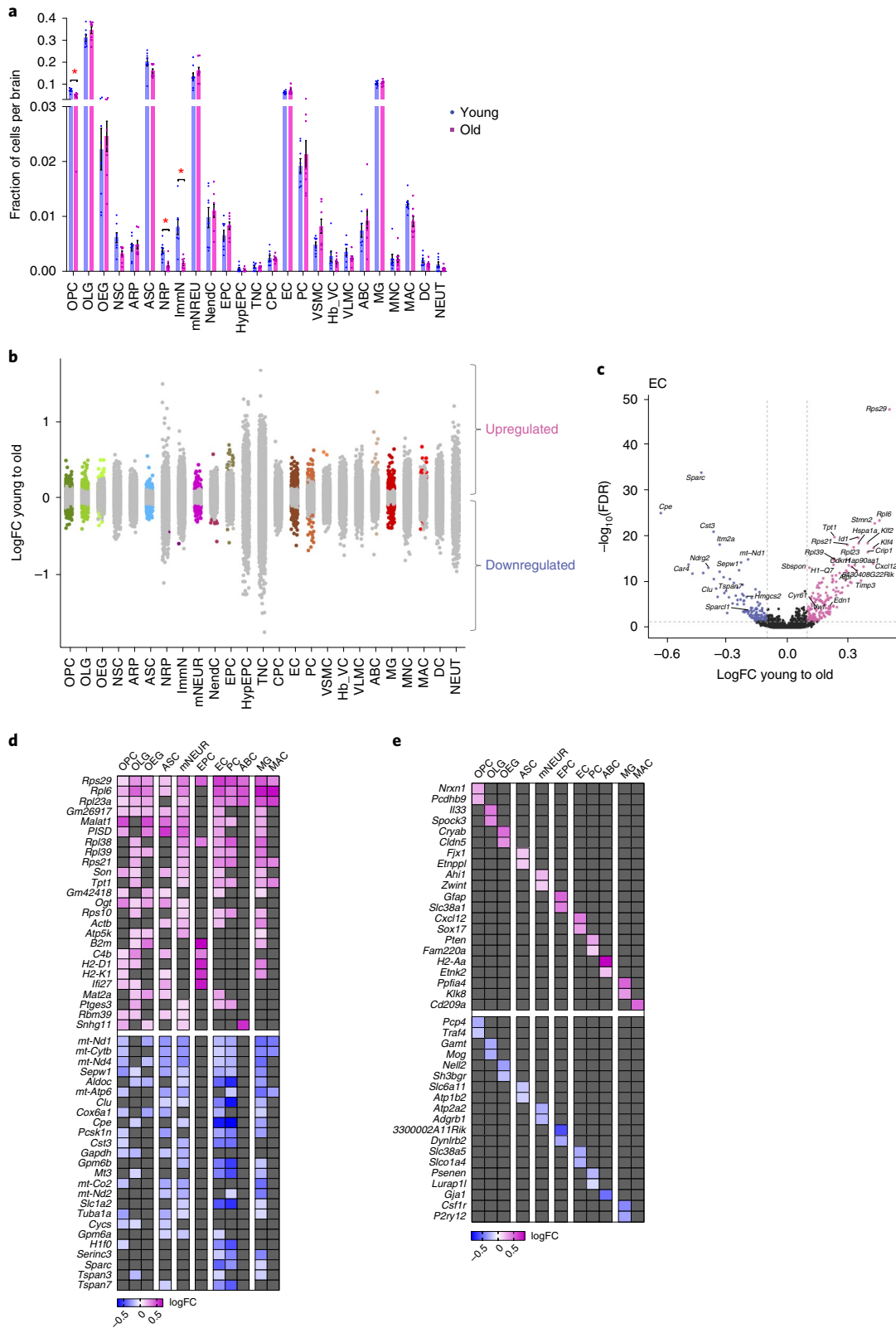


Fig. 2 | Aging-related population shifts and changes in gene expression. a, Bar plot showing the fraction of cells associated with each cell type in both young and old brains (data present mean \pm s.e.m. of 8 young and 8 old brains; *FDR < 0.05 by two-tailed Mann-Whitney *U*-test). **b**, Strip chart showing the aging-related logarithmic FCs (logFC) of all detected genes (dots) across all 25 cell types. Genes in colored dots are significantly (FDR < 0.05 and FC > 10%) upregulated or downregulated with aging, as determined by MAST analysis (see details in Methods). Genes in gray are not significantly changed with aging. **c**, Sample volcano plot for EC showing $-\log_{10}(\text{FDR})$ and logFC values for all genes with highlighting for those that are significantly upregulated (magenta dots) or downregulated (blue dots) with aging. Genes in black are not significantly changed with aging. **d**, Heatmap of logFC showing a subset of aging-related genes (FDR < 0.05 and FC > 10%) that are shared across many of the major cell types. Gray indicates no significant change with aging. **e**, Heatmap of logFC showing a subset of aging-related genes (FDR < 0.05 and FC > 10%) that are unique to each major cell type.

an established clustering algorithm¹¹. Next, we removed clusters likely to be of low quality, resulting from debris, doublets/multiplets and dead cells (Supplementary Fig. 3) and used other critical quality control steps as described in the Methods section (Supplementary Fig. 4). Ultimately, our analysis led to the identification of 37,069 cells (Supplementary Fig. 5a), representing 25 cell types (Fig. 1b), with distinct expression profiles (Fig. 1c,d and Supplementary Fig. 6): oligodendrocyte precursor cells (OPC), oligodendrocytes (OLG), olfactory ensheathing glia (OEG), neural stem cells (NSC), astrocyte-restricted precursors (ARP), astrocytes (ASC), neuronal-restricted precursors (NRP), immature neurons (ImmN), mature neurons (mNEUR), neuroendocrine cells (NendC), ependymocytes (EPC), hypendymal cells (HypEPC), tanycytes (TNC), choroid plexus epithelial cells (CPC), endothelial cells (EC), pericytes (PC), vascular smooth muscle cells (VSMC), hemoglobin-expressing vascular cells (Hb-VC), vascular and leptomeningeal cells (VLMC), arachnoid barrier cells (ABC), microglia (MG), monocytes (MNC), macrophages (MAC), dendritic cells (DC) and neutrophils (NEUT). Cell counts and other metrics for each cell type are shown in Fig. 1e and Supplementary Fig. 5b–e.

Identification of cell subtypes and states. To reveal heterogeneity within each population, we grouped the aforementioned cell types into 6 classes based on their expression profile, lineage, function and anatomical organization (oligodendrocyte lineage, astrocyte lineage and stem cells, neuronal lineage, ependymal cells, vasculature cells and immune cells) (Supplementary Fig. 7) and used another round of clustering. This subsetting of the data enabled us to highlight more subtle changes within the classes without the impact of variation due to inclusion of drastically different cell identities. This secondary analysis identified dozens of different cell subtypes and states reflecting distinct functional, maturational and regional cell identities (Supplementary Fig. 8–9). These cell identities are in line with recent scRNA-seq studies^{12–14}, whose purpose was to identify novel and distinct cell types/subtypes and create detailed atlases of the developing and adult mouse brain (see details in Supplementary Fig. 8). This process allowed us to generate a comprehensive dataset of gene expression profiles for all the experimentally validated cell populations from both young and old brains at high resolution (Supplementary Tables 1 and 2). It also permitted us to identify specific markers that distinguish each type regardless of age (Supplementary Tables 3 and 4).

Aging-related effects on cell-to-cell transcriptional variability and cellular composition. We found that cell identity is largely preserved in old brains as indicated by unbiased clustering where all clusters represent cells of all animals from both ages (Supplementary Fig. 4c). Furthermore, the quality of data generated from both young and old cell types appears similar, with each having

comparable numbers of unique molecular identifiers (UMI) and detected genes (Supplementary Fig. 5c,e). Next, we compared the coefficient of variation of expression for all the transcribed genes (Supplementary Fig. 10a), only the mitochondrially encoded genes (Supplementary Fig. 10b) or only the ribosomal protein genes (Supplementary Fig. 10c). We observed differences in the variability of transcription between young and old cells in many cell types. However, the directionality of change was not identical among cell types, providing evidence that aging is not broadly associated with increased transcriptional variation¹⁵.

Then, by investigating the abundance of each cell type, we found that cellular composition was largely consistent across both young and old brains (Fig. 2a and Supplementary Table 5). Nonetheless, we were able to confirm the previously reported aging-related decline of OPC¹⁶, NRP¹⁷ and ImmN^{17,18} (Fig. 2a) and to reveal potentially interesting but not statistically significant population shifts within certain subtypes of OPC, OLG, ASC, mNEUR and MG (Supplementary Fig. 11; see also Supplementary Fig. 8). Of note, although the estimated percentages for each cell type do not necessarily reflect their actual proportions in the mouse brain, mainly due to differences in their sensitivity to tissue dissociation, the observed changes in cell-type ratios appear to reflect a real biological effect.

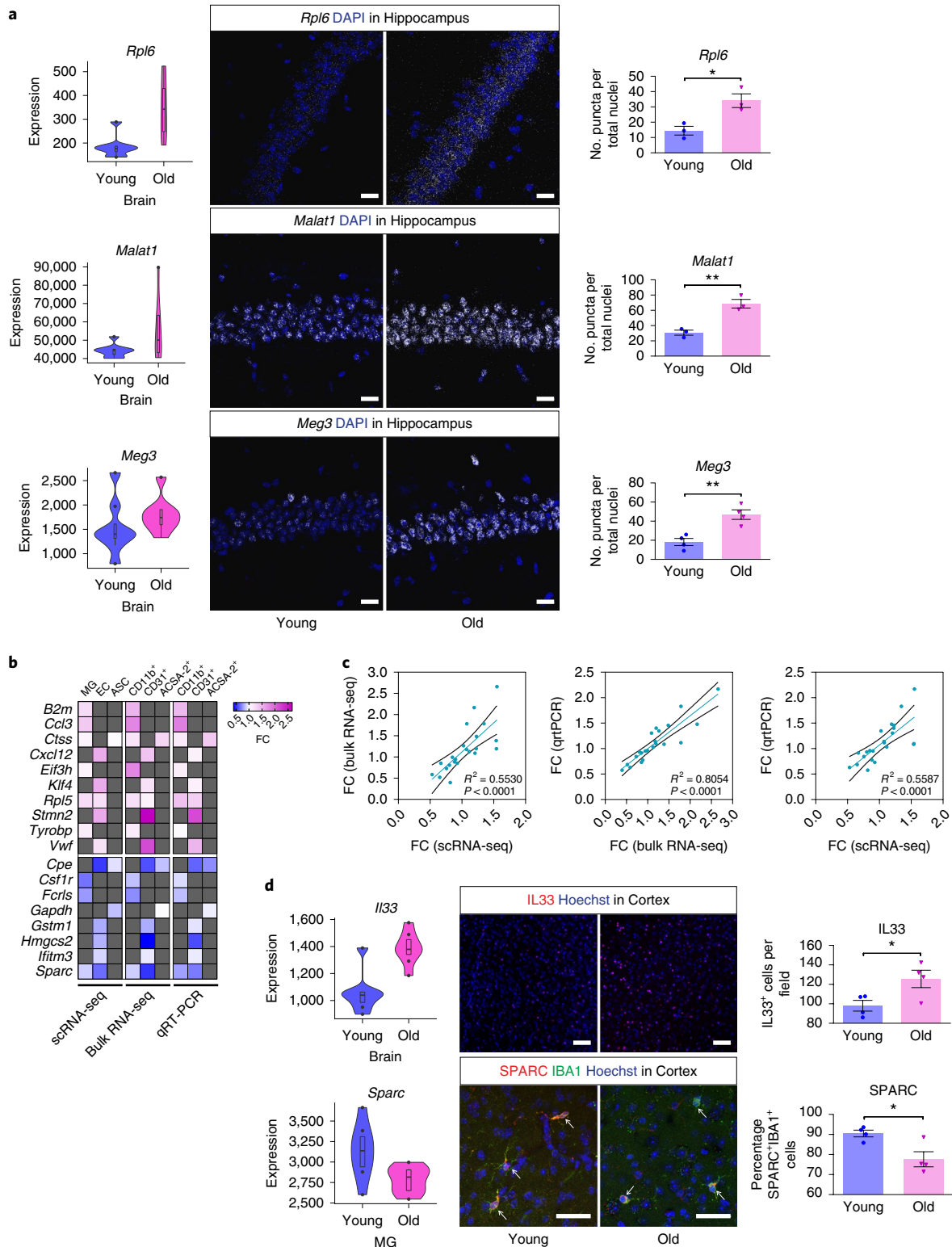
Identification of aging-related genes. We then investigated the breadth of transcriptional changes that occur in the mouse brain with aging by performing differential gene expression (DGE) analysis between young and old cell types and neuronal subtypes (Supplementary Tables 6 and 7). Of the 14,699 total detected genes, 3,897 were significantly affected by aging in at least one cell type (false-discovery rate (FDR) < 0.05). When the magnitude of change in expression was also considered, 1,113 genes passed the 10%-fold-change (FC) threshold (Fig. 2b and Supplementary Table 8). Interestingly, of those, 1,027 exhibited the same directionality regardless of the cell-type identity (531 upregulated and 496 downregulated), while the direction of change in the expression of 86 genes was different across cell populations (discussed further below; Supplementary Table 8). As described in the Methods section, our ability to identify genes whose transcription changes significantly with aging and the calculation of FC is dependent on several factors, including the number of cells within each population, the level of transcription and the algorithm for analysis.

Identification of shared and cell-type specific aging signatures. To ensure the validity of these aging signatures, we first started broadly and compared our data with past transcriptomic studies of the mouse aging brain^{4–6}. To more effectively compare datasets, we aggregated all of our sequenced cells, thereby recreating a traditional whole-brain profile similar to what might be observed with bulk sequencing (Supplementary Tables 2 and 6). As expected, this

Fig. 3 | Validation of shared and cell-type-specific aging-related gene expression changes. **a**, Violin plots with boxplots overlaid with data in TPM from our scRNA-seq across all cells derived from each brain ($n = 16$ brains; 8 young and 8 old) (left) and RNAscope in situ hybridization images of mouse hippocampi (middle) showing the aging-related upregulation of the ribosomal protein gene *Rpl6* and of the lncRNAs *Malat1* and *Meg3*. Scatter plots (right) showing the quantification of the RNAscope data (data presents mean \pm s.e.m. of 3 young and 3 old brains for *Rpl6* and *Malat1* and of 4 young and 4 old brains for *Meg3*; $*P = 0.0279$ for *Rpl6*, $**P = 0.0082$ for *Malat1*, $**P = 0.0045$ for *Meg3* by two-tailed Welch's *t*-test). Scale bar, 20 μ m. **b**, Heatmap showing the FCs of a few representative significantly (FDR < 0.05) aging-related genes in MG, EC and ASC as identified by our scRNA-seq (left) and verified by both bulk RNA-seq (middle) and qRT-PCR (right) on sorted CD11b⁺ (MG), CD31⁺ (EC) and ACSA-2⁺ (ASC) cells. Gray indicates no aging-related gene expression changes in the sequencing data; consequently, these genes were not analyzed by qRT-PCR. For the qRT-PCR experiments, data presents mean \pm s.e.m. of 3–9 young and 3–10 old brains. **c**, Scatter plots showing the significant correlations of the gene expression changes in **b** between the scRNA-seq, bulk RNA-seq and qRT-PCR datasets. Linear regression is depicted by the colored line, while black dotted lines represent 95% confidence intervals. Pearson's squared correlation coefficient (R^2) and the P value are shown at the bottom right of each plot. **d**, Violin plots with boxplots overlaid with data in TPM from our scRNA-seq ($n = 16$ brains; 8 young and 8 old) (left) and immunohistochemistry images of mouse cortices (middle) showing the aging-related upregulation of IL33 (that is mainly expressed in OLG; see Supplementary Fig. 14) and the aging-related downregulation of SPARC in MG (IBA1⁺ cells; indicated by arrows). Scatter plots (right) showing the quantification of the immunohistochemistry data (data presents mean \pm s.e.m. of 4 young and 4 old brains; $*P = 0.0467$ for IL33⁺ cells, $*P = 0.0342$ for SPARC⁺/IBA1⁺ cells by two-tailed Welch's *t*-test). Scale bar, 50 μ m.

analysis verified previously identified aging-related genes (such as *B2m*, *C4b*, *Ctss*, *Il33*, *Rpl8*). Moreover, due to the increased sensitivity of the techniques used in our study compared to past ones, we were able to identify a set of aging-related genes not reported previously (such as *Apoc1*, *Caly*, *Cxcl12*, *Nell2*, *Ybx1*; see Supplementary Table 6). These changes could have been masked in past studies due to their limited expression levels or variations in less-abundant cell populations. Importantly, our single-cell DGE

data enabled us to build on these results to identify from which cell types these aging signatures arose. For example, *Ctss*, while highly transcribed in all immune cells (MG, MAC, MNC, DC; see Supplementary Table 2), was only significantly changed with aging in MG (Supplementary Table 6). Another example is *Nell2*, which is mostly transcribed in neuronal lineage cells and OEG (Supplementary Table 2), but its levels changed with aging only in OEG (Supplementary Table 6).



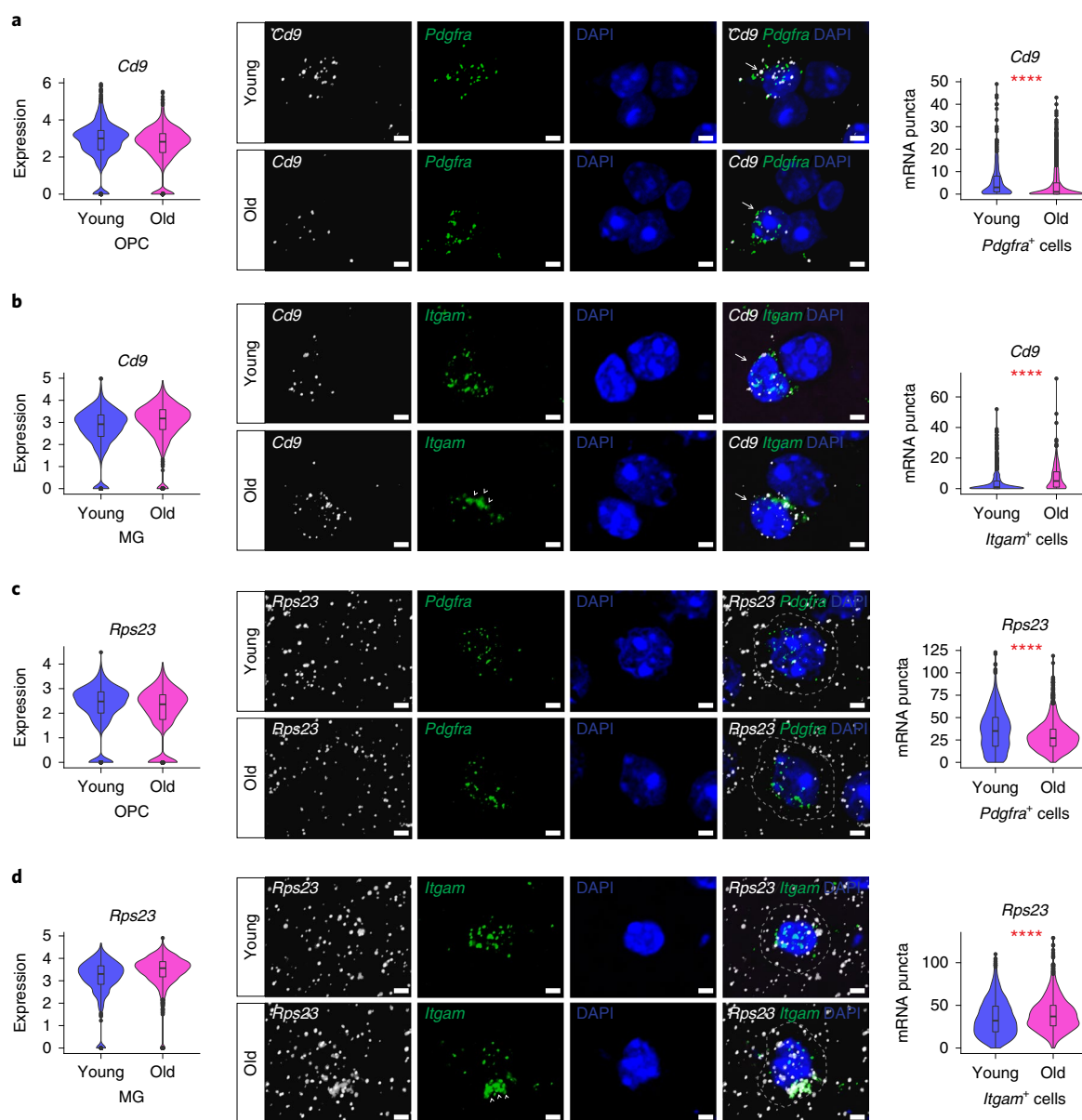


Fig. 4 | Validation of bidirectional aging-related gene expression changes. **a, b**, Violin plots with boxplots overlaid with data in UMI from our scRNA-seq (left) and RNAscope in situ hybridization micrographs of mouse cortices (middle) showing the aging-related downregulation of *Cd9* in OPC (*Pdgfra*⁺ cells; indicated by arrows) (**a**) and the aging-related upregulation of the same gene in MG (*Itgam*⁺ cells; indicated by arrows) (**b**). Arrowheads in **b** designate autofluorescence from lipofuscin granules in the lysosomes of old MG (see details in Methods). Violin plots with boxplots overlaid (right) showing the quantification of the RNAscope data (data presents median expression of *Cd9* in *Pdgfra*⁺ OPC ($n = 529$ cells from 4 young brains, $n = 1,922$ cells from 4 old brains) and *Itgam*⁺ MG ($n = 841$ cells from 4 young brains, $n = 3,058$ cells from 4 old brains); **** $P < 0.0001$ by two-tailed Mann-Whitney *U*-test). Scale bar, 2 μm . **c, d**, Violin plots with boxplots overlaid with data in UMI from our scRNA-seq (left) and RNAscope in situ hybridization micrographs of mouse cortices (middle) showing the aging-related downregulation of the ribosomal protein gene *Rps23* in OPC (**c**) and the aging-related upregulation of the same gene in MG (**d**). As in **b**, arrowheads in **d** designate autofluorescence from lipofuscin granules. Dotted lines outline the area of each cell that was considered for quantification (see details in Methods). Violin plots with boxplots overlaid (right) showing the quantification of the RNAscope data (data presents median expression of *Rps23* in *Pdgfra*⁺ OPC ($n = 1,012$ cells from 4 young brains, $n = 2,483$ cells from 4 old brains) and *Itgam*⁺ MG ($n = 1,234$ cells from 4 young brains, $n = 2,237$ cells from 4 old brains); **** $P < 0.0001$ by two-tailed Mann-Whitney *U*-test). Scale bar, 2 μm .

We then focused our analysis on 11 major cell populations that exhibited the greatest number of differentially regulated genes (Fig. 2b). By comparing the DGE data from these populations (Fig. 2c and Supplementary Fig. 12), we were able to distinguish both shared and cell-type-specific aging signatures. Supplementary Table 8 presents a matrix that specifies the genes that changed significantly in each cell type.

Figure 2d presents selected top aging-related genes that are shared across multiple cell types. The majority of the most commonly aging-upregulated genes were ribosomal protein genes (such as *Rpl6*), lncRNA genes (such as *Malat1*) and immunoregulatory/inflammatory genes (such as *B2m*). The most commonly aging-downregulated genes were mitochondrial respiratory chain complex genes (such as *mt-Nd1*), glycolysis-related genes (such as

Aldoc) and genes encoding selenoproteins (such as *Sepw1*) (see also Supplementary Table 8).

A subset of genes representing cell-type-specific aging signatures are highlighted in Fig. 2e. Interestingly, these data revealed that certain genes that are traditionally used as cell-type-specific markers change with aging, such as the decrease of *Mog* in OLG and *Csf1r* in MG, and the increase of *Cxcl12* in EC. Conversely, we observed that other classic cell-type marker genes change with aging in other cell populations. For example, *Gfap*, which is highly transcribed and enriched in the astrocyte lineage and stem cells (Supplementary Table 2), was found as one of the genes that increased the most in EPC (Fig. 2e and Supplementary Tables 6 and 8).

We next sought to validate certain shared and cell-type unique aging-related gene expression changes. As shown in Fig. 3a, we were able to verify transcriptional changes in the shared aging-related genes *Rpl6*, *Malat1* and *Meg3* by *in situ* hybridization. We also confirmed the cell-type specific aging-related changes of genes such as *Csf1r*, *Cxcl12* and *Sparc* by bulk RNA-seq and quantitative reverse-transcription PCR (qRT-PCR analysis) of fluorescence-activated cell sorting (FACS)-purified CD31⁺ (EC), CD11b⁺ (MG) and ACSA-2⁺ (ASC) cells (Fig. 3b,c and Supplementary Fig. 13). Additionally, to further determine if our transcriptomic approach faithfully captured changes at the protein level, we performed immunohistochemistry. As shown in Fig. 3d, we indeed observed the specific aging-related downregulation of SPARC in MG and the global aging-related increase of IL33 that is mostly expressed by OLG (Supplementary Fig. 14), as revealed by our scRNA-seq analysis (Fig. 2e and Supplementary Table 2) and by others^{19,20}.

Identification of bidirectional aging signatures. Analysis of our sequencing dataset also revealed individual genes with opposite regulation among different cell types (Supplementary Fig. 15 and Supplementary Table 8). For example, the tetraspanin *Cd9* was downregulated in OPC and ASC but upregulated in EC and MG. This bidirectional aging signature was confirmed between OPC and MG by dual fluorescence *in situ* hybridization (Fig. 4a,b). Another example of bidirectional changes with aging is *Cldn5*, which is often used as a marker for EC, but it is also highly transcribed in OEG (Supplementary Table 2). We found aging-related downregulation of *Cldn5* in EC but upregulation in OEG (Supplementary Table 6). Notably, when its levels were measured in the whole brain, changes were minimal (Supplementary Tables 2 and 6), further highlighting why certain changes were masked in previous bulk sequencing studies.

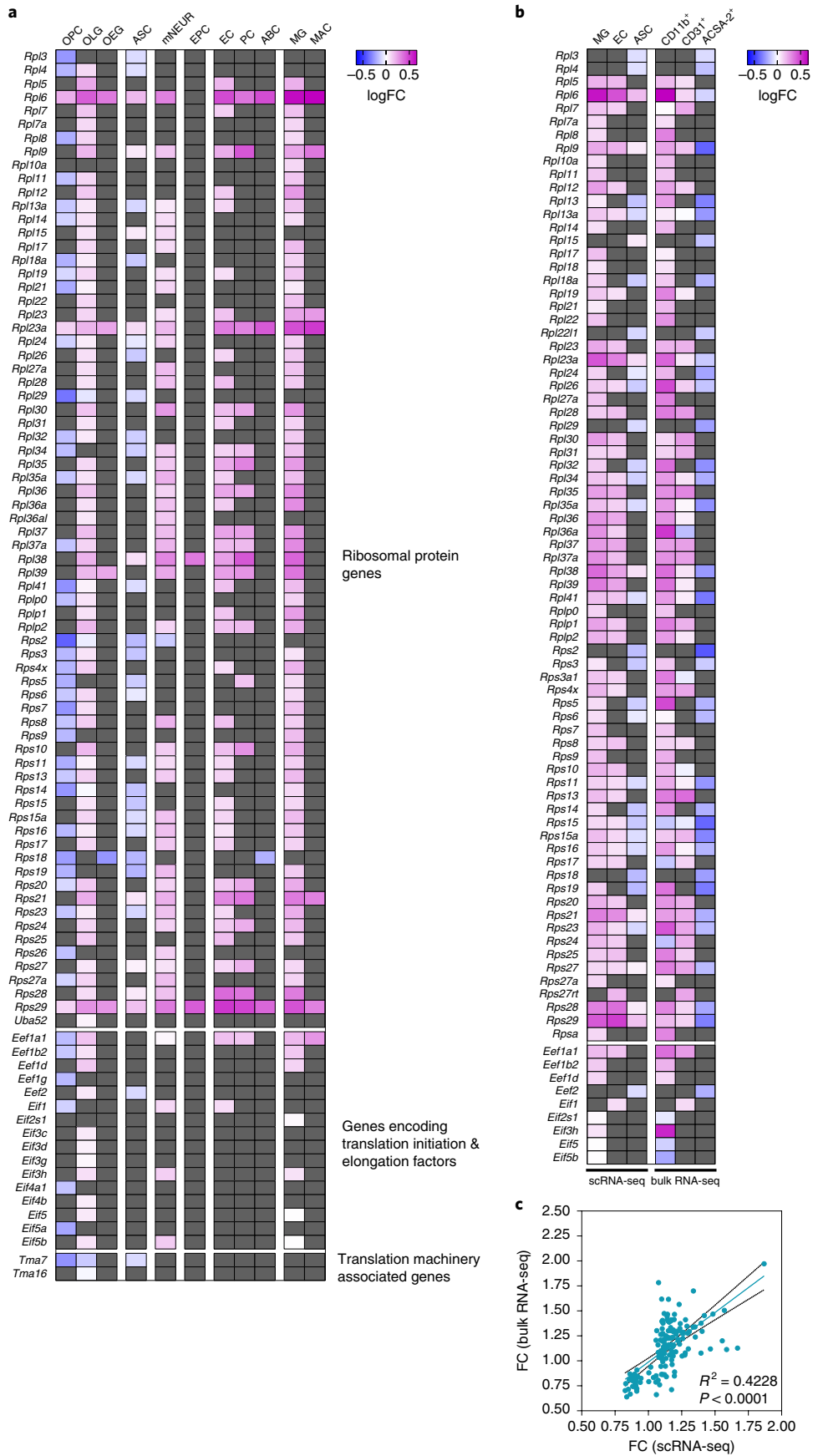
Similarly, we found large gene sets, such as ribosomal protein genes, that were discordant between cell types (Supplementary Fig. 15b). As mentioned above, many ribosomal protein genes were found among the top shared aging-upregulated genes across major cell populations (Fig. 2d and Supplementary Table 8), but a subset of these genes also exhibited differential regulation/directionality with aging in certain cell types (Supplementary Fig. 15b). For example, *Rps23* was found to be downregulated in OPC and ASC, but upregulated in mNEUR, EC and MG. This differential aging-related transcriptional signature was confirmed in OPC and MG by dual fluorescence *in situ* hybridization (Fig. 4c,d).

Interestingly, when we examined the expression profile of all genes encoding ribosomal proteins across major cell populations, we found two distinct and divergent patterns. As shown in Fig. 5a (see also Supplementary Table 8), both OPC and ASC were found to downregulate a fraction of their ribosomal protein genes with aging, while the other cell types upregulated their expression. These patterns of expression were also detected when neuronal subtypes were compared, where GABA and GLUT neurons exhibited upregulation of their ribosomal protein genes with aging, while DOPA neurons exhibited downregulation (Supplementary Table 7). To validate these broad bidirectional aging-related signatures, we examined ribosomal protein gene expression in FACS-purified ACSA-2⁺ (ASC), CD31⁺ (EC) and CD11b⁺ (MG) cells. As shown in Fig. 5b,c, bulk RNA-seq reproduced the scRNA-seq data for a subset of ribosomal protein genes, highlighting their potentially distinct responses to aging.

Identification of aging-related pathways. Next, we investigated changes in aging-related cellular pathways and processes by performing gene set enrichment analysis (GSEA)²¹. GSEA has increased sensitivity compared to DGE analysis as it aggregates information from broad sets of genes that are presumed to be functionally related. As such, we were also able to include cell types and neuronal subtypes with limited cell numbers that did not show significant aging-related changes by DGE analysis. This approach revealed the existence of many shared and cell-type specific aging-related pathways across the examined cell populations (Fig. 6 and Supplementary Tables 9 and 10). In total, 451 pathways (1,142 GSEA terms) changed significantly ($P < 0.05$ and $q < 0.25$); 234 were expressed in at least 2 cell types, while the remaining 217 were unique for specific cell populations. Of those aging-related pathways, 339 exhibited the same directionality regardless of cell type (195 were upregulated and 144 downregulated), while the directions of change in the remaining 112 varied across cell types (Supplementary Table 10). The most common aging-related pathways were those associated with cellular respiration, protein synthesis, inflammatory response, oxidative stress and growth factor signaling (Fig. 6 and Supplementary Table 10). As expected, GSEA showed that the aging process entails many biological changes in mNEUR that were in common across its major subtypes. These include the impairment of key metabolic pathways, the dysregulation of ion homeostasis and the disruption of neurotransmission (Supplementary Tables 9 and 10), all of which have been well documented in the literature³.

Here, we highlight changes in EC and EPC, two understudied, but important, brain cell populations, that form the barriers that isolate the brain parenchyma from factors circulating in blood and cerebrospinal fluid. GSEA showed that EC exhibit numerous aging-related changes in cellular pathways, such as the induction of senescence, hypoxia signaling and response to ketone signaling, and the reduction of xenobiotic metabolism, lipid metabolism and hormone processing (Supplementary Fig. 16a and Supplementary Tables 9 and 10). In EPC, there was a notable upregulation of interferon-induced signaling (Supplementary Fig. 16b and Supplementary Tables 9 and 10) that aligns with the

Fig. 5 | Aging-related changes in the expression of ribosomal protein genes. **a**, Heatmap showing the logFC for all the significantly (FDR < 0.05) aging-related ribosomal and translation-associated genes across 11 cell types, as identified by our scRNA-seq. Gray indicates no significant change with aging. **b**, Heatmap of logFC showing all the significant (FDR < 0.05) aging-related ribosomal protein genes and translation-associated genes across MG, EC and ASC as identified by our scRNA-seq (left) and further verified by bulk RNA-seq on sorted CD11b⁺ (MG), CD31⁺ (EC) and ACSA-2⁺ (ASC) cells (right). The few inconsistencies presented here more probably reflect differences in the composition of the input sorted populations used for the comparisons (see details in the Methods section). **c**, Of note, despite the fact that only a subset of these genes was found significantly dysregulated in our bulk RNA-seq analysis, due to lower statistical power, there is a significant correlation of the gene expression changes between the scRNA-seq and bulk RNA-seq datasets, as shown in the scatter plot. More specifically, dots in **c** represent all genes from the examined cell types in **b**. Linear regression is depicted with the colored line, while black dotted lines represent 95% confidence intervals. Pearson's squared correlation coefficient (R^2) and P value are shown at the bottom right of the plot.



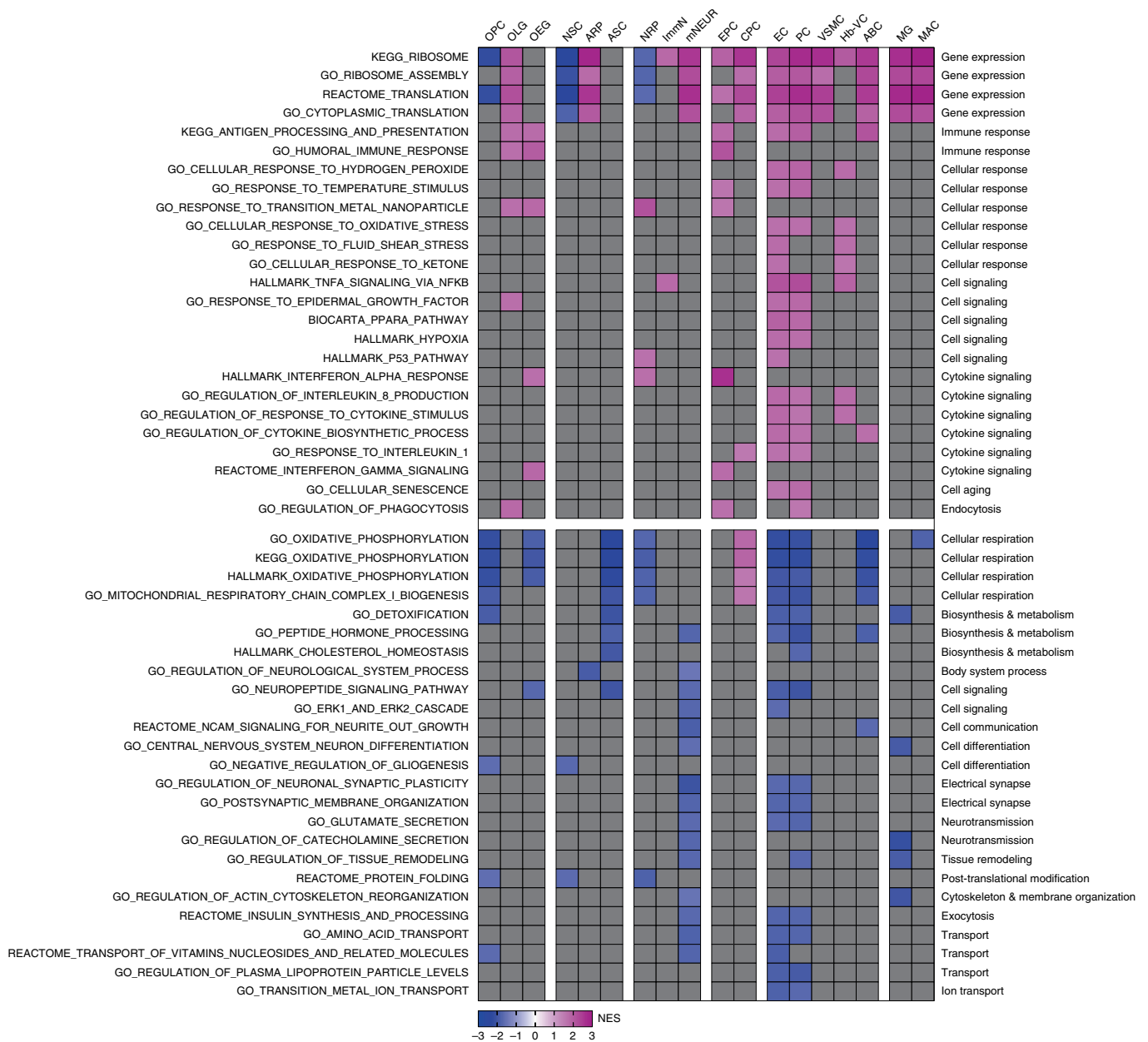


Fig. 6 | Aging-related changes in cellular pathways and processes. Heatmap of GSEA showing a small subset of significant ($P < 0.05$ and $q < 0.25$) aging-related pathways across major cell types. Numbers in legend correspond to normalized enrichment scores (GSEA statistics; see details in Methods). Positive normalized enrichment score values indicate upregulation, while negative normalized enrichment score values indicate downregulation. Gray indicates no significant change with aging.

induction of certain interferon-stimulated genes (like *Ifitm3*) just as found in the DGE analysis (Supplementary Tables 6 and 8). The aging-related upregulation of interferon-stimulated genes and other aging-induced genes was also seen by qRT-PCR in FACS-purified EPC (Supplementary Fig. 17). This finding suggests that an aging-induced inflammatory response may extend to these cells and appears similar to what it has been previously reported for the choroid plexus epithelium²⁷.

Importantly, GSEA also points to ribosome biogenesis as a biological process exhibiting differential regulation with aging across different cell types and neuronal subtypes, beyond what we found with DGE analysis alone (Supplementary Tables 9 and 10). In particular, even with stringent significance criteria, the vast majority of brain cell types was seen to exhibit an aging-related upregulation of genes encoding ribosomal subunits, while three types of stem/

progenitor cells (NSC, NRP, OPC) showed downregulation (Fig. 6, Supplementary Fig. 18 and Supplementary Table 10).

Identification of aging-related changes in intercellular communication. Finally, our single-cell transcriptomics data provides the ability to explore how aging-driven changes in gene expression might affect intercellular communication within the brain. By leveraging the transcriptional profiles of each cell population, we built a comprehensive intercellular network of potential ligand–receptor interactions among nearly all the identified brain cell types. We then enriched this network with data from our DGE analysis to mark all those interactions that were found to change with aging at the ligand or receptor level.

Here we highlight the ligand–receptor changes in EC (Fig. 7), not only because they exhibited a variety of aging-related changes,

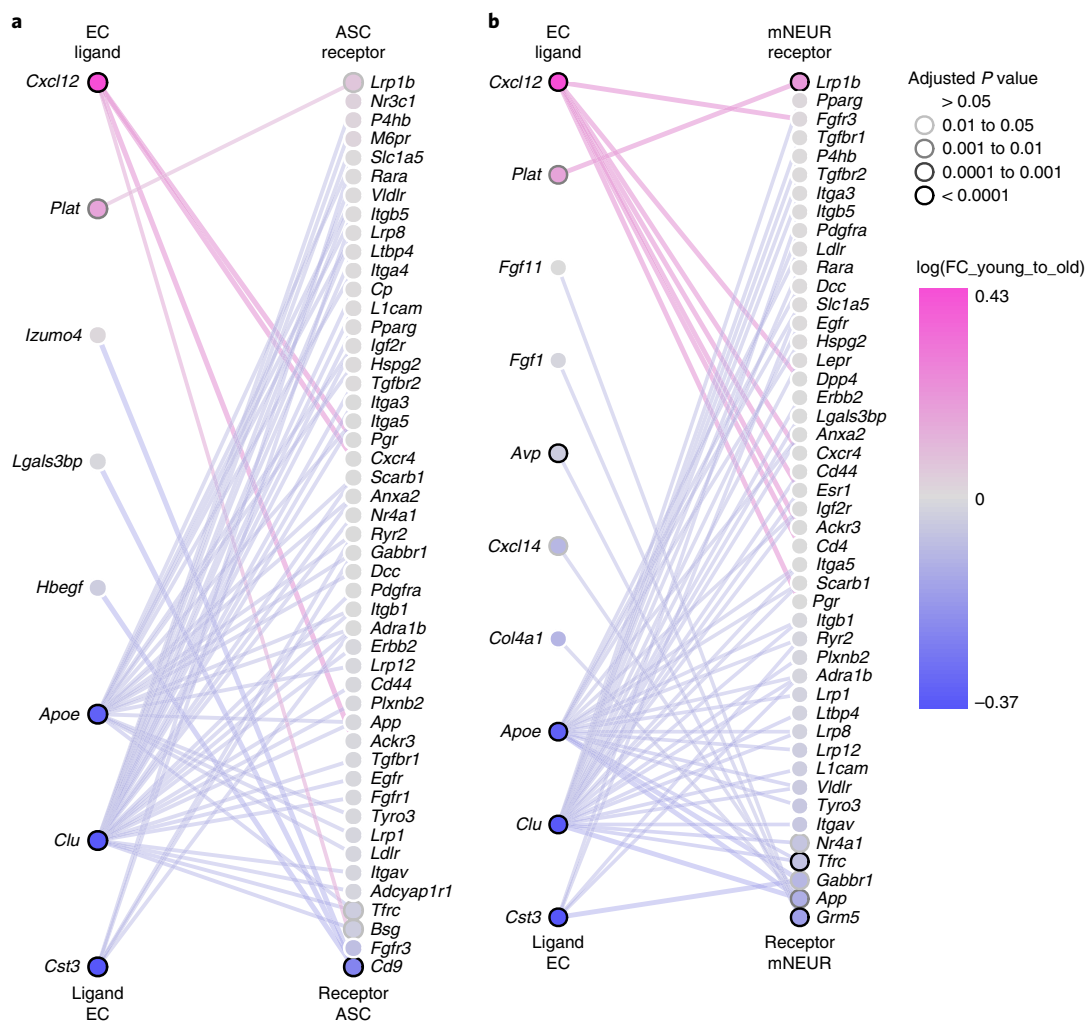


Fig. 7 | Aging-related changes in intercellular communication. **a, b**, Aging-related ligands produced and secreted by EC with receptors expressed in ASC (**a**) and aging-related ligands produced and secreted by EC with receptors expressed in mNEUR (**b**). In both panels, nodes represent ligands or receptors expressed in the denoted cell type, and edges represent protein-protein interactions between them. Node color represents magnitude of DGE (logFC as estimated by the MAST model), such that the most significantly age-upregulated genes are in magenta and age-downregulated are in blue. Node borders indicate statistical significance of differential expression, specifically the FDR (padj) expected from the MAST analysis. Edge color represents the sum of scaled differential expression magnitudes from each contributing node, while width and transparency are determined by the magnitude of scaled differential expression (see details in the Methods section). These figures have been filtered such that the top 65 edges representing the most differentially expressed node pairs are shown. Figures for these cell interactions, and all others, are available from our online interactive data viewer accessible at <http://shiny.baderlab.org/AgingMouseBrain/>.

as mentioned above (Fig. 2b,c and Supplementary Fig. 16a), but also because they possess the unique ability to interact directly with factors synthesized in the brain and with those secreted by peripheral tissues into the circulation. Network analysis showed that both cystatin C (*Cst3*, an aging-downregulated gene) and stromal cell-derived factor 1 (*Cxcl12*, an aging-upregulated gene), which have been previously linked to multiple pathologies^{23,24}, are mediators of crosstalk between vascular cells and many brain cell types (Fig. 7). This finding signifies that their aging-related changes may modulate, either synergistically or separately, important, but still-to-be-identified aging-related processes occurring in the brain parenchyma.

Discussion

In this study, we first investigated the cellular complexity of the mouse brain and showed that cell identity and composition is generally maintained with aging. More specifically, we found that the numbers of cells within most of the cell types did not change

radically with age, when quantified as a fraction of total brain cells. Nonetheless, we did observe the previously reported aging-related decline of certain cell populations, such as NRP¹⁷. Of note, it seems possible that additional work focused on this issue might reveal additional changes in subtypes of cells, particularly those occurring in specific regions of the brain.

We then compared young and old cells and observed a noticeable aging-related cell-to-cell transcriptional variation within certain cell populations. However, our data did not show a universal aging-related change in transcriptional variability across all cell types. That is, gene transcription in particular cell populations does not necessarily become more variable with aging. This finding is in line with Warren et al.²⁵ but in contrast to other studies that suggested increased transcriptional variability as a common feature of aging^{15,26}.

By aggregating all of our sequenced single cells and performing DGE analysis comparable to what was done in previous bulk sequencing studies, we validated many of the previously identified

aging-related genes^{4–6} and extended the list to include additional gene signatures. We then used single-cell-type DGE analyses to reveal the primary cell type(s) generating these signatures. The fine resolution provided by scRNA-seq further allowed us to detect changes in specific cell populations that would otherwise be masked by bulk sequencing techniques. More specifically, single-cell-type DGE analyses yielded a large number of aging-related genes that are (1) commonly regulated among cell types, (2) specific to certain cell types and (3) discordant between cell types. To the best of our knowledge, only a small fraction of the genes reported here have been previously associated with brain aging.

Interestingly, our data analysis revealed different patterns of aging across cell populations. We found that certain aging-related genes and pathways are differentially regulated across cell types. For example, we provide evidence that, with aging, expression of ribosomal protein genes is regulated in opposite directions among groups of cell types and among neuronal subtypes. Data from both DGE and pathway analyses showed that most of the brain cell types exhibited an aging-driven upregulation of ribosomal protein genes, while those exhibiting the opposite regulation include important stem/progenitor cell populations. This paradoxical bidirectional regulation of ribosomal protein genes with aging is noteworthy.

Over the past years, it has been clearly shown that the attenuation of protein synthesis by dietary restriction or genetic manipulation of translation-associated genes, including those encoding ribosomal subunits, increases the lifespan of multiple species²⁷. Notably, the downregulation of ribosomal protein genes and bulk protein synthesis has been long considered as a hallmark of aging²⁸. It appears that the aging-driven downregulation of ribosomal protein genes had been widely accepted, mostly based on transcriptomic studies in yeast²⁸. However, several studies in other model organisms and humans have presented conflicting results^{5,29–35}. Zahn et al. reported an aging-driven upregulation of ribosomal protein genes in human brain and muscle tissues³⁵ and, in a later study, reported an aging-driven upregulation of ribosomal protein genes in mouse neuronal tissues⁵ with a downregulation of the same genes in multiple nonneuronal tissues⁵. Moreover, recently published transcriptomic studies showed an aging-related downregulation of ribosomal protein genes in ASC⁷ and NSC³⁶ and an upregulation in MG of both aged^{37,38} and diseased brains^{37,39,40}. Intriguingly, a very recent study reported increased ribosome biogenesis and activity as hallmarks of premature aging in human fibroblasts⁴¹. A possible explanation for this is that cells with different metabolic demands are affected differently by aging, thus inducing alternative feedback loops to partially compensate for loss of translational efficiency and protein synthesis. Another explanation is that certain cell populations may start producing different types and/or levels of specialized ribosomes⁴² tailored to their translational needs to cope with the metabolic changes induced by aging.

Collectively, these data indicate that the aging process may not be identical in all cell types, which is in line with our findings and with a recent transcriptome analysis of the *Drosophila melanogaster* brain that showed a differential aging trajectory in the transcriptional profile of neurons and glial cells³³. In short, it is not yet clear whether the regulation of ribosomal protein genes and other translation-associated genes is causative of aging or the consequence of physiological changes accompanying aging, or both depending on species, tissue and cell type. However, our work demonstrating that ribosome biogenesis is one of the aging-related pathways that is differentially regulated across cell types may help to reconcile seemingly conflicting studies.

Lastly, we created a roadmap of intercellular communication in the brain by generating detailed information on ligand–receptor interactions that change with aging across nearly all brain cell types. This roadmap is also of high importance as recent findings from

our lab⁴³ and others^{22,44} have shown that certain secreted factors, either derived from brain parenchyma or blood, are able to modulate brain aging, degeneration and rejuvenation. Thus, the discovery of novel factors, their source, and their targets are emerging areas of importance in the aging field². We foresee the extension of this network by including data from blood proteomic analyses and transcriptomic data from both disease models and heterochronic parabiosis experiments⁴³ that may help in identifying novel therapeutic targets for treating functional defects in the brain brought on by aging and disease.

Our findings, in agreement with recent studies, highlight the sensitivity and power of single-cell transcriptomics not only to reveal differences in cell identities but also to reveal changes within individual cell types after different treatments and conditions^{20,45,46}, including organismal aging^{8,9,32–34,38,47}. As single-cell sequencing technologies continue to mature, some of the technical and experimental limitations that we encountered will be improved upon. These include (1) potential sampling problems resulting from the enzymatic dissociation of the brain that may be overcome with single-nuclei sequencing approaches¹⁹; (2) potential age-associated biases in response to dissociation, cell encapsulation and other procedures that might drive transcriptional differences between experimental groups; (3) the relatively small number of cells sequenced compared to the total size of the brain, restricting the comparative analyses to more abundant cell populations; (4) the relatively shallow depth of sequencing, limiting the analysis to highly transcribed genes; and (5) the lack of full-length splicing isoform profiling that could be enabled with other methods⁴⁸. Our data could not also reveal potentially important aging-driven regional changes⁴⁹ that may be resolved with spatial mapping sequencing approaches⁵⁰ or sex-specific gene expression variations, as only whole brain preparations of male mice were analyzed.

Nonetheless, our work identified aging-related changes in nearly all mouse brain cell types and revealed different patterns of aging across different populations, many of which we validated in this study. Thus, while there may be hallmarks of aging that occur in most cell types, such as mitochondrial dysfunction and loss of proteostasis^{1,3,28}, our data argue against the hypothesis that aging induces a single universal molecular program in all cells and tissues¹⁰. However, we note that the aging process may occur gradually or in discrete steps depending on complex interactions among cells in the brain and ways in which these interactions are modified by extrinsic factors, such as stress and exercise. Thus, future studies exploring gene expression changes along a continuum, by examining additional timepoints, will help to reveal the precise aging trajectories for each cell and gene and to distinguish changes that are causative of aging from those that change as a consequence of aging.

Collectively, as a resource for the neuroscience community and to those who study the biology of aging, we provide comprehensive datasets of genes, pathways and ligand–receptor interactions with aging-related variation for all the mouse brain cell types identified. We expect that, beyond the valuable exploration of aging signatures and novel insights regarding the aging process, our data will be used as a reference for a series of other applications. For example, we showed that numerous putative cell-specific marker genes change with aging. Thus, the purification or investigation of cells, based on single discriminatory markers, may be faulty in the context of aging. Similarly, our data revealed that the transcript levels of certain housekeeping genes change with aging in many cell types, which could confound some quantitative analyses.

Overall, these data will help to advance a variety of efforts towards understanding and modulating the aging process and exploring molecular and cellular therapeutic targets for aging-related neurodegenerative diseases.

Online content

Any methods, additional references, Nature Research reporting summaries, source data, statements of code and data availability and associated accession codes are available at <https://doi.org/10.1038/s41593-019-0491-3>.

Received: 10 October 2018; Accepted: 9 August 2019;
Published online: 24 September 2019

References

- Lopez-Otin, C., Blasco, M. A., Partridge, L., Serrano, M. & Kroemer, G. The hallmarks of aging. *Cell* **153**, 1194–1217 (2013).
- Wyss-Coray, T. Ageing, neurodegeneration and brain rejuvenation. *Nature* **539**, 180–186 (2016).
- Mattson, M. P. & Arumugam, T. V. Hallmarks of brain aging: adaptive and pathological modification by metabolic states. *Cell Metab.* **27**, 1176–1199 (2018).
- Lee, C. K., Weindruch, R. & Prolla, T. A. Gene-expression profile of the ageing brain in mice. *Nat. Genet.* **25**, 294–297 (2000).
- Zahn, J. M. et al. AGEMAP: a gene expression database for aging in mice. *PLoS Genet.* **3**, e201 (2007).
- de Magalhaes, J. P., Curado, J. & Church, G. M. Meta-analysis of age-related gene expression profiles identifies common signatures of aging. *Bioinformatics* **25**, 875–881 (2009).
- Clarke, L. E. et al. Normal aging induces A1-like astrocyte reactivity. *Proc. Natl Acad. Sci. USA* **115**, E1896–E1905 (2018).
- Hammond, T. R. et al. Single-cell RNA sequencing of microglia throughout the mouse lifespan and in the injured brain reveals complex cell-state changes. *Immunity* **50**, 253–271 (2018).
- Kalamakis, G. et al. Quiescence modulates stem cell maintenance and regenerative capacity in the aging brain. *Cell* **176**, 1407–1419.e1414 (2019).
- de Magalhaes, J. P. Programmatic features of aging originating in development: aging mechanisms beyond molecular damage? *FASEB J.* **26**, 4821–4826 (2012).
- Xu, C. & Su, Z. Identification of cell types from single-cell transcriptomes using a novel clustering method. *Bioinformatics* **31**, 1974–1980 (2015).
- Zeisel, A. et al. Molecular architecture of the mouse nervous system. *Cell* **174**, 999–1014.e1022 (2018).
- Saunders, A. et al. Molecular diversity and specializations among the cells of the adult mouse brain. *Cell* **174**, 1015–1030.e1016 (2018).
- Rosenberg, A. B. et al. Single-cell profiling of the developing mouse brain and spinal cord with split-pool barcoding. *Science* **360**, 176–182 (2018).
- Bahar, R. et al. Increased cell-to-cell variation in gene expression in ageing mouse heart. *Nature* **441**, 1011–1014 (2006).
- Sim, F. J., Zhao, C., Penderis, J. & Franklin, R. J. The age-related decrease in CNS remyelination efficiency is attributable to an impairment of both oligodendrocyte progenitor recruitment and differentiation. *J. Neurosci.* **22**, 2451–2459 (2002).
- Walter, J., Keiner, S., Witte, O. W. & Redeker, C. Age-related effects on hippocampal precursor cell subpopulations and neurogenesis. *Neurobiol. Aging* **32**, 1906–1914 (2011).
- Ben Abdallah, N. M., Slomianka, L., Vyssotski, A. L. & Lipp, H. P. Early age-related changes in adult hippocampal neurogenesis in C57 mice. *Neurobiol. Aging* **31**, 151–161 (2010).
- Habib, N. et al. Massively parallel single-nucleus RNA-seq with DroNc-seq. *Nat. Methods* **14**, 955–958 (2017).
- Hrvatin, S. et al. Single-cell analysis of experience-dependent transcriptomic states in the mouse visual cortex. *Nat. Neurosci.* **21**, 120–129 (2018).
- Subramanian, A. et al. Gene set enrichment analysis: a knowledge-based approach for interpreting genome-wide expression profiles. *Proc. Natl Acad. Sci. USA* **102**, 15545–15550 (2005).
- Baruch, K. et al. Aging. Aging-induced type I interferon response at the choroid plexus negatively affects brain function. *Science* **346**, 89–93 (2014).
- Li, M., Hale, J. S., Rich, J. N., Ransohoff, R. M. & Lathia, J. D. Chemokine CXCL12 in neurodegenerative diseases: an SOS signal for stem cell-based repair. *Trends Neurosci.* **35**, 619–628 (2012).
- Mathews, P. M. & Levy, E. Cystatin C in aging and in Alzheimer's disease. *Ageing Res. Rev.* **32**, 38–50 (2016).
- Warren, L. A. et al. Transcriptional instability is not a universal attribute of aging. *Aging Cell* **6**, 775–782 (2007).
- Martinez-Jimenez, C. P. et al. Aging increases cell-to-cell transcriptional variability upon immune stimulation. *Science* **355**, 1433–1436 (2017).
- Gonskikh, Y. & Polacek, N. Alterations of the translation apparatus during aging and stress response. *Mech. Ageing Dev.* **168**, 30–36 (2017).
- Frenk, S. & Houseley, J. Gene expression hallmarks of cellular ageing. *Biogerontology* **19**, 547–566 (2018).
- Sun, D. et al. Epigenomic profiling of young and aged HSCs reveals concerted changes during aging that reinforce self-renewal. *Cell Stem Cell* **14**, 673–688 (2014).
- Kowalczyk, M. S. et al. Single-cell RNA-seq reveals changes in cell cycle and differentiation programs upon aging of hematopoietic stem cells. *Genome Res.* **25**, 1860–1872 (2015).
- Peters, M. J. et al. The transcriptional landscape of age in human peripheral blood. *Nat. Commun.* **6**, 8570 (2015).
- Enge, M. et al. Single-cell analysis of human pancreas reveals transcriptional signatures of aging and somatic mutation patterns. *Cell* **171**, 321–330.e314 (2017).
- Davie, K. et al. A single-cell transcriptome atlas of the aging drosophila brain. *Cell* **174**, 982–998.e20 (2018).
- Angelidis, I. et al. An atlas of the aging lung mapped by single cell transcriptomics and deep tissue proteomics. *Nat. Commun.* **10**, 963 (2019).
- Zahn, J. M. et al. Transcriptional profiling of aging in human muscle reveals a common aging signature. *PLoS Genet.* **2**, e115 (2006).
- Leeman, D. S. et al. Lysosome activation clears aggregates and enhances quiescent neural stem cell activation during aging. *Science* **359**, 1277–1283 (2018).
- Holtman, I. R. et al. Induction of a common microglia gene expression signature by aging and neurodegenerative conditions: a co-expression meta-analysis. *Acta Neuropathol. Commun.* **3**, 31 (2015).
- Olah, M. et al. A transcriptomic atlas of aged human microglia. *Nat. Commun.* **9**, 539 (2018).
- Keren-Shaul, H. et al. A unique microglia type associated with restricting development of Alzheimer's disease. *Cell* **169**, 1276–1290.e1217 (2017).
- Mathys, H. et al. Temporal tracking of microglia activation in neurodegeneration at single-cell resolution. *Cell Rep.* **21**, 366–380 (2017).
- Buchwalter, A. & Hetzer, M. W. Nucleolar expansion and elevated protein translation in premature aging. *Nat. Commun.* **8**, 328 (2017).
- Steffen, K. K. & Dillin, A. A ribosomal perspective on proteostasis and aging. *Cell Metab.* **23**, 1004–1012 (2016).
- Katsimpardi, L. et al. Vascular and neurogenic rejuvenation of the aging mouse brain by young systemic factors. *Science* **344**, 630–634 (2014).
- Villeda, S. A. et al. Young blood reverses age-related impairments in cognitive function and synaptic plasticity in mice. *Nat. Med.* **20**, 659–663 (2014).
- Campbell, J. N. et al. A molecular census of arcuate hypothalamus and median eminence cell types. *Nat. Neurosci.* **20**, 484–496 (2017).
- Wu, Y. E., Pan, L., Zuo, Y., Li, X. & Hong, W. Detecting activated cell populations using single-cell RNA-Seq. *Neuron* **96**, 313–329.e316 (2017).
- Dulken, B. W. et al. Single-cell analysis reveals T cell infiltration in old neurogenic niches. *Nature* **571**, 205–210 (2019).
- Gupta, I. et al. Single-cell isoform RNA sequencing characterizes isoforms in thousands of cerebellar cells. *Nat. Biotechnol.* **36**, 1197–1202 (2018).
- Spitzer, S. O. et al. Oligodendrocyte progenitor cells become regionally diverse and heterogeneous with age. *Neuron* **101**, 459–471.e455 (2019).
- Rodrigues, S. G. et al. Slide-seq: a scalable technology for measuring genome-wide expression at high spatial resolution. *Science* **363**, 1463–1467 (2019).

Acknowledgments

We acknowledge T. Okino and his team at Ono Pharmaceuticals for fruitful discussions and useful suggestions during the progress of this work. We are grateful to F. Rapino, N. Rodriguez-Muela, K. Pfaff, A. Freeman and J. LaLonde for their helpful advice in different aspects of our work and/or for reviewing the manuscript. We also thank the staff members of the Harvard Bauer Core Facility, the Harvard Center for Biological Imaging and the Harvard Stem Cell and Regenerative Biology Histology Core for their technical advice and assistance. The work was supported by Ono Pharmaceutical Co., Ltd (L.L.R.), the Stanley Center for Psychiatric Research and the Klarman Cell Observatory (J.Z.L.). The funders had no role in the study design, experiments performed, data collection, data analysis and interpretation, or preparation of the manuscript.

Author contributions

M.X., S.L.L., S.M.B. and L.L.R. conceived the study. M.X., S.L.L., S.M.B., J.Z.L. and L.L.R. designed the study. M.X., X.A., D.D. and L.N. performed the scRNA-seq experiments. S.L.L., S.K.S. and J.Z.L. processed the scRNA-seq data. M.X. and S.L.L. analyzed the scRNA-seq data. B.T.I. and G.D.B. created the ligand-receptor interaction network. M.X. and V.L.B. performed the bulk RNA-seq experiments. S.L.L. and V.L.B. processed the bulk RNA-seq data. M.X. and S.L.L. analyzed the bulk RNA-seq data. M.X. and Z.N. performed the flow cytometry experiments. M.X. performed the qRT-PCR experiments. M.X. and B.A.M. performed the RNAscope ISH experiments. M.X. and C.O. performed the IHC experiments. R.I. and G.D.B. provided the cell-cell interaction dataset. M.X., S.L.L., S.S.L., A.R., G.D.B. and J.Z.L. supervised aspects of the study. L.L.R. supervised the whole study. J.Z.L. and L.L.R. secured funding. M.X. wrote the original draft of the manuscript. S.L.L., S.M.B. and L.L.R. edited the manuscript. All authors reviewed the manuscript and approved its submission.

Competing interests

The authors declare no competing interests.

Additional information

Supplementary information is available for this paper at <https://doi.org/10.1038/s41593-019-0491-3>.

Correspondence and requests for materials should be addressed to M.X. or L.L.R.

Peer review information *Nature Neuroscience* thanks Mark Cookson and the other, anonymous, reviewer(s) for their contribution to the peer review of this work.

Reprints and permissions information is available at www.nature.com/reprints.

© The Author(s), under exclusive licence to Springer Nature America, Inc. 2019

Methods

Animals. C57BL/6J mice (JAX no. 000664) were housed in the Harvard Bioblab Animal Facility under standard conditions. All experimental procedures were approved in advance by the Animal Care and Use Committee of Harvard University (AEP no. 10–23) and are in compliance with federal and state laws. Young male mice were used at 2–3 months of age, and old male mice at 21–22 months of age.

Brain tissue dissociation. Brain tissue harvest and dissociation was performed at the same time (09:00–10:00) for each animal, thus limiting circadian variation⁵¹. For brain tissue dissociation, we modified existing protocols and developed a new one that enables the isolation of intact living cells from both young and old mouse brains in less than 1 h. Briefly, mice were CO₂ anesthetized and then rapidly decapitated. Brains were extracted, and hindbrain regions were removed. The remaining tissue was dissociated into single cells with the Adult Brain Dissociation kit (Miltenyi Biotec no. 130-107-677) with these modifications: (1) the tissue was manually dissociated following the basic steps of the protocol described in the Neural Tissue Dissociation Kit (Miltenyi Biotec no. 130-092-628); (2) 5% (w/v) trehalose (Sigma Aldrich no. T0167) was added in all buffers to ensure higher cellular viability⁵²; (3) half concentration of papain was used, and the digestion was performed at 33–35°C; (4) the enzymatic reaction was quenched with ovomucoid protease inhibitor, as described in the Papain Dissociation System (Worthington no. LK003182); (5) cell clusters were removed by serial filtration through prewetted 70- μ m (Falcon no. 352350) and 40- μ m (Falcon no. 352340) nylon cell strainers; (6) myelin debris and erythrocyte removal steps were omitted to prevent any bias in the recovered cell yields; (7) all centrifugations were performed at 220g for 8 min at 4°C. After dissociation, cells were kept on ice for no longer than 1 h until further processing.

Single-cell RNA sequencing. For the scRNA-seq experiments, 8 young and 8 old mouse brains were analyzed, with 2 animals killed per day. Brain cells were processed through all steps to generate stable cDNA libraries. Briefly, after dissociation, cells were diluted in ice-cold PBS containing 0.4% BSA at a density of 1,000 cells μ l⁻¹. For every sample, 17,400 cells were loaded into a Chromium Single Cell 3' Chip (10x Genomics) and processed following the manufacturer's instructions. Then, scRNA-seq libraries were prepared with the Chromium Single Cell 3' Library & Gel Bead kit v2 and i7 Multiplex kit (10x Genomics). Libraries were pooled based on their molar concentrations. Pooled libraries were then loaded at 2.07 pM and sequenced on a NextSeq 500 instrument (Illumina) with 26 bases for read1, 57 bases for read2 and 8 bases for Index1. Cell Ranger (v.1.2) (10x Genomics) was used to perform sample de-multiplexing, barcode processing and single-cell gene-UMI counting, while a digital expression matrix was obtained for each experiment with default parameters⁵³, mapped to the 10X reference for mm10, v.1.2.0. After the initial sequencing, the samples in each pool were re-pooled based on the actual number of cells detected by Cell Ranger (Supplementary Fig. 2a), to sequence each sample to a similar depth (number of reads/cell) (median, 40,007; Supplementary Fig. 2c). Multiple NextSeq runs were conducted to achieve over 70% sequencing saturation as determined again by Cell Ranger (median, 75%; Supplementary Fig. 2f).

Raw data processing and quality control for cell inclusion. Basic processing and visualization of the scRNA-seq data were performed with the Seurat package (v.2.3) in R (v.3.3.4)^{54–56}. Our initial dataset contained 50,212 cells with data for 19,607 genes. The average numbers of UMI (nUMI) and nonzero genes (nGene) were 2,876.70 and 1,112.56, respectively. The data were log normalized and scaled to 10,000 transcripts per cell. Variable genes were identified with the FindVariableGenes() function with the following parameters used to set the minimum and maximum average expression and the minimum dispersion: x.low.cutoff = 0.0125, x.high.cutoff = 3, y.cutoff = 0.5. Next, principal component analysis (PCA) was carried out, and the top 20 principal components (PCs) were stored, which is the default number in Seurat. Clusters were identified with the FindClusters() function by use of the shared nearest neighbor modularity optimization with a clustering resolution set to 1.6. All clusters with only one cell were removed. This method resulted in 40 initial clusters. Data for all cells are provided in Supplementary Fig. 3a with colors representing each of the clusters. For initial quality-control filtering, we selectively removed entire clusters, with the majority of cells having greater than 30% mitochondrial RNA, under 1,000 detected transcripts, or under 500 unique genes. Finally, we filtered the remaining individual cells with the following parameters: minimum percentage mito = 0, maximum percentage mito = 30%, minimum number of UMI = 200, maximum number of UMIs = 30,000, minimum number of nGene = 250, and maximum number of nGene = 6,000 to exclude outliers. Finally, we removed any genes that were only detected in fewer than 3 cells. After initial quality control, we maintained a total of 38,244 cells and 14,699 genes. Data for all cells are provided in Supplementary Fig. 3b with black representing excluded cells and gray the included cells. The average nUMI, nonzero genes, percentage mitochondrial RNA, and percentage ribosomal RNA were 3,199.12, 1,284.08, 8.33% and 6.94%, respectively. PCA was again carried out, and the top 20 PCs were retained. The clustering was again performed with the clustering resolution now set to 2.0.

This method resulted in 55 initial clusters. The final preprocessing stage was to remove likely doublet artifacts arising from the co-capture of multiple cells in one droplet. This step occurred following an initial round of determination of cell-type identity as described in the next section. We first searched for the top differential markers for each identified cluster/sub-cluster using the FindMarkers() function (Supplementary Tables 3 and 4). Then, we defined doublets/multiplets as any cluster in which >30% of its cells express at least 5 of the top 10 genes specific for the initially identified cell type and any other cell type outside of the cell class it is associated with (see below for details on cell classes). These clusters were removed from downstream analysis. Furthermore, cell clusters that were not represented by at least half of the young and old animals were also excluded. For example, although we detected epithelial cells (*Epcam*⁺/*Krt18*⁺) in our dataset, we excluded them from our processing as they were detected only in two of the eight young animals but none of the old animals. After exclusions, clustering was again performed. Ultimately, we included 37,069 cells representing 38 clusters (Supplementary Fig. 4).

Determination of cell-type identity. For each cell type, we used multiple cell-type-specific/enriched marker genes that have been previously described in the literature to determine cell-type identity. These include, but are not limited to *Pdgfra* for OPC⁵⁷; *Cldn11* for OLG⁵⁷; *Npy* for OEG^{14,58}; *Thbs4* for NSC^{59–63}; *Cd44* for ARP⁶⁴; *Gja1* for ASC⁶⁵; *Cdk1* for NRP; *Sox11* for ImmN⁶⁵; *Syt1* for mNEUR⁶⁶; *Baiap3* for NendC⁶⁷; *Ccdc153* for EPC⁶⁵; *Sspo* for HypEPC¹²; *Rax* for TNC⁶⁵; *Thr* for CPC⁶⁸; *Cldn5* for EC⁶⁹; *Kcnj8* for PC⁶⁹; *Acta2* for VSMC⁶⁹; *Alas2* for Hb-VC^{20,70}; *Slc6a13* for VLMC^{12,57}; *Slc47a1* for ABC¹²; *Tmem119* for MG⁴⁶; *Plac8* for MNC⁷¹; *Pf4* for MAC⁷¹; *Cd209a* for DC^{71,72}; *S100a9* for NEUT⁷¹ (see Fig. 1c,d). We then arranged all the identified cell types based on their expression profile, lineage, function and anatomical organization into 6 classes of cells (Supplementary Fig. 7a). For each class, we re-clustered the subcategorized cell types following the same strategy (top 20 PCs with a clustering resolution of 2.0). Only for the neuronal lineage, which has an increased complexity in terms of cell subtypes, we used the top 40 PCs to yield more separated clusters. The annotation of subclusters was performed similarly to identification of the main cell clusters, with additional reported cell type/subtype marker genes^{73–76}.

DGE analysis. After initial quality-control preprocessing and determination of cellular identities, we used the MAST package (v.1.6.1)⁷⁷ in R (v.3.3.4) to perform DGE analysis. MAST generated *P* values, FCs and logFC (based on natural log of the FCs), using a hurdle model with normalized nUMI as a covariate. It is worth mentioning that due to shrinkage in the Bayes approach leveraged by MAST, we were able to detect significance in very small changes in transcription but there was also an underestimation of FC. This effect is especially noticeable when comparing FC between MAST calculations and traditional TPM-based calculations for genes with low expression levels. Additionally, the DGE techniques used here have more power to assign significance of subtle changes in highly transcribed genes, and therefore our results may underrepresent changes in lowly transcribed genes. Finally, our ability to establish a baseline level of transcription is proportional to the number of cells measured, and thus more subtle changes in abundant populations can be deemed significant.

Pathway analysis. GSEA²¹ was performed to identify cellular pathways and processes associated with aging. Analysis was carried out with the GSEA package (v.3.0) (Broad Institute), following the protocol described by Reimand et al.⁷⁸. Briefly, before the analysis, genes for every distinct cell population were ranked according to their DGE changes and significance (young versus old). Two preranked gene lists were generated for each cell population: (1) with all genes transcribed, and (2) without the highly abundant mitochondrially encoding genes and ribosomal protein genes. All these preranked gene lists were then used as an input, while 5 gene datasets (Hallmark pathways, GO biological processes, KEGG, BioCarta, Reactome (v.6.1)) were used as a reference. To calculate the *P* values for each pathway, 1,000 random permutations were performed. Only gene sets with *P* < 0.05 and *q* < 0.25 were considered as significantly enriched. To overcome redundancy and help interpretation of the analysis, we grouped terms overrepresenting the same pathway using the Cytoscape software (v.3.5.1) and the AutoAnnotate app (v.1.2)⁷⁹. Pathways belonging to similar biological processes were also grouped together for easier navigation/exploration (Supplementary Tables 9 and 10). For the expression heatmaps of pathways and processes, the top leading edge genes and their raw normalized expression values were determined by the Cytoscape software (v.3.5.1) and the EnrichmentMap app (v.3.0)⁷⁹. More specifically, for each gene value (TPM) in a row of expression, the mean of the row was subtracted and then divided by the row's standard deviation.

Intercellular network analysis. Cell–cell interactions were predicted by a method similar to that described by Kirouac et al.⁸⁰. First, a cell communication interactome was created, collecting known protein–protein interactions between receptor, ligand and extracellular matrix (ECM) proteins. Receptor genes were defined based on a set of GO terms (GO: 0043235, receptor complex; GO: 0008305, integrin complex; GO: 0072657, protein localized to membrane; GO: 0043113, receptor clustering; GO: 0004872, receptor activity; GO: 0009897, external side of

plasma membrane) and UniProt (search term: "Receptor [KW-0675]" GO: 0005886 organism: human). Ligand genes were defined based on a GO term (GO: 0005102, receptor binding) and the set of proteins labeled as secreted in the Secretome dataset (<https://www.proteinatlas.org/humanproteome/secretome>)⁸¹. ECM genes were defined based on a set of GO terms (GO: 0031012, extracellular matrix; GO: 0005578, proteinaceous extracellular matrix; GO: 0005201, extracellular matrix structural constituent; GO: 1990430, extracellular matrix protein binding; and GO: 0035426, extracellular matrix cell signaling). Gene lists were manually curated to correct or remove genes that were misclassified. With the curated list of receptors, ligands and ECM genes, known protein–protein interactions were collected from iRefindex (v.14)⁸², Pathway Commons (v.8)⁸³ and BioGRID (v.3.4.147)⁸⁴, keeping only those occurring between genes from the different classes (ligand, receptor, ECM). This dataset is available at <https://baderlab.org/CellCellInteractions>. To predict cell–cell interactions, the ligand–receptor interaction dataset was filtered for genes detected to be expressed at the mRNA transcription level in our cell types. To investigate aging-related perturbations in these putative cell–cell interaction networks, DGE metrics from the MAST analysis outlined above were used to build subnetworks for each set of interactions between cell types. In these networks, nodes represent ligands or receptors expressed in the denoted cell type, and edges represent protein–protein interactions between them. Nodes were colored to represent the magnitude of DGE (logFC as estimated by the MAST model). These values were scaled per cell type and summed to determine edge weight. An R Shiny application was built to interactively explore the bipartite graphs generated from this analysis and is available at <http://shiny.baderlab.org/AgingMouseBrain/> and on GitHub at <https://github.com/BaderLab/AgingMouseBrainCCInx>.

Flow cytometry. For the simultaneous isolation and purification of ASC, EC and MG, we developed a multicolor flow cytometry approach. Briefly, dissociated cells from each brain were pelleted (220g, 8 min, 4°C) and resuspended in 1 ml of ice-cold labeling buffer (HBSS without calcium and magnesium, 0.1% BSA, 2 mM EDTA, 5% trehalose, 1% GlutaMAX). Cells were incubated with 100 µl of FcR blocking reagent (Miltenyi Biotec no. 130-092-575) for 12 min at 4°C under continuous rotation and then labeled with 3 µg ml⁻¹ of each of the following antibodies: APC anti-ACSA-2 (Miltenyi Biotec no. 130-102-315) for ASC; BV786 anti-CD31 (BD Biosciences no. 740870 and BD Biosciences no.740879) for EC; and BV510 anti-CD11b (BD Biosciences no.562950) for MG. Cells were also incubated with the following antibodies targeting unwanted cell populations: PE anti-CD200 (BioLegend no. 123808) for mNEUR and Alexa Fluor 488 anti-O4 (R&D Systems no. FAB1326G) for OLG. This step is critical as it helps to exclude unwanted cells during sorting, thus minimizing cross-contamination events. After 12 min of incubation at 4°C (in dark conditions), cells were washed extensively, pelleted and resuspended in ice-cold FACS buffer (HBSS containing calcium and magnesium, 0.5% BSA, 5% trehalose, 1% Glutamax) in a volume of 25 ml per brain (5 FACS tubes). To exclude cellular debris and dead cells, 15 min before sorting, 10 µM Calcein Blue AM (BD Biosciences no. 564060) was added to the FACS tubes to stain live cells. Calcein⁺ cells were then sorted with a MoFlo Astrios instrument (Beckman Coulter) with a 70 µm nozzle at 60 psi. Gates were set manually with compensation beads (Life Technologies no. A10497) and appropriate control samples, and data were analyzed with FlowJo software (v.10). For the purification of EPC, we followed a similar flow cytometry approach using these antibodies: APC anti-CD133 (Miltenyi Biotec no. 130-102-197); APC anti-CD133 (eBioscience no. 17-1331-81); PE anti-CD24a (BD Biosciences no. 553262); and PE anti-CD24a (BioLegend no. 138504). To minimize RNA degradation, sorted cells were collected directly in RL buffer (Norgen Biotek no. 48500) supplemented with 10% BME, in a 1:1 final ratio (50% lysis buffer: 50% cells in sheath fluid; the PBS-based solution that is derived from the flow cytometer). After sorting, cell lysates were snap frozen and stored at –80°C for up to 1 month until further processing.

RNA extraction. Total RNA was extracted from sorted cells with the total RNA purification plus Micro kit (Norgen Biotek no. 48500) following the manufacturer's instructions. Before RNA extraction, a chloroform extraction step was included to remove myelin debris/lipids, as well as an on-column DNase digestion step (Qiagen no. 79254) to remove genomic and mitochondrial DNA. For all samples, RNA concentration was determined with a Qubit Fluorometer (Invitrogen), while RNA purity and integrity were evaluated with a BioAnalyzer instrument (Agilent). After extraction, RNA was immediately stored at –80°C for no longer than a month until further processing.

Bulk RNA sequencing. For the bulk RNA-seq experiments, sorted/purified cells from 8 mouse brains (4 young and 4 old) were analyzed. Bulk RNA-seq was performed with a modified version of the SCRIB-Seq that was originally developed for single-cell RNA-seq analysis⁸⁵. Briefly, polyadenylated RNA, from total RNA (7.5–25 ng; RNA integrity number (RIN) values > 6.5) extracted from our FACS-purified cells, with ERCC Spike-in control Mix A (Ambion) at 10⁻⁶ final dilution, was converted to cDNA and decorated with universal adapters, sample-specific barcodes and UMI with a template-switching reverse transcriptase. Decorated cDNA was then pooled, amplified and prepared for multiplexed sequencing (NextSeq 500, Illumina) with a modified transposon-based fragmentation approach that enriched for 3' ends and preserved strand information.

Bulk sequencing data analysis. Postsequencing quality control on each of the libraries was performed to assess coverage depth, enrichment for messenger RNA (exon/intron and exon/intergenic density ratios), fraction of rRNA reads and number of detected genes with bespoke scripts. Second sequence reads were aligned against the murine genome mm9 with bwa mem (v.0.7.10-r789) (<http://bio-bwa.sourceforge.net/>). Gene expression was estimated based on reads mapping near the 3' end of transcripts with ESAT⁸⁶, based on the mm9 Refseq annotation, with flags java -Xmx128G -task score3p -wLen 50 -wExt 5000 -wOlap 0 -sigTest 0.01 -multimap ignore. Results were summarized as counts per million mapped reads, merged across samples, log transformed and subjected to hierarchical clustering and visualization. For ERCC quantification, reads were mapped against the ERCC sequences by use of STAR (v.2.5.1b)⁸⁷ with flags --runMode alignReads --runThreadN 8 --outSAMtype BAM SortedByCoordinate --outFilterType BySJout --outFilterMultimapNmax 20 --outFilterMismatchNmax 999 --alignIntronMin 10 --alignIntronMax 1000000 --alignMatesGapMax 1000000 --alignSJoverhangMin 8 --alignSJDBoverhangMin 1 --quantMode TranscriptomeSAM. Bam files from STAR were sorted and indexed with samtools⁸⁸, and counts were retrieved from the indices with idxstats. DGE analysis⁸⁹ was performed in R (v.3.2.3) with Bioconductor's DESeq2 package (v.3.7)⁹⁰. Dataset parameters were estimated with the estimateSizeFactors() and estimateDispersions() functions; read counts across conditions were modeled based on a negative binomial distribution, and a Wald test was used to test for differential expression (nbinomWaldtest()), all packaged into the DESeq() function with the age as a contrast.

Quantitative reverse transcription PCR. For the qRT-PCR experiments, sorted/purified cells from 19 mouse brains (9 young and 10 old) were analyzed. Briefly, RNA samples with RIN values > 6.5 were reverse transcribed into cDNA with the iScript cDNA synthesis kit (Bio-Rad no. 170-8891) following the manufacturer's instructions. The resulting cDNA was then processed for qRT-PCR analysis with predesigned primers (Integrated DNA Technologies) (Supplementary Table 1) and the Fast SYBR Green Master Mix (Life Technologies no. 4385614) in a QuantStudio 12 K Flex Real-Time PCR System (Applied Biosystems). Before data analysis, we examined the melting curves for each reaction and included only those with a single peak at the expected melting temperature. The FC in gene expression was determined by the 2^{-DDCT} method⁹¹, and all values were normalized to the endogenous expression of *Vcp*; a housekeeping gene that has been proposed for calibration in quantitative experiments⁹². Our scRNA-seq analysis showed that in the vast majority of cell populations *Vcp* levels remain unaltered with aging, in contrast to other more commonly used genes. Samples with *Vcp* Ct values > 29 were excluded from our analysis. Each sample was repeated in technical duplicates on 3–10 biological replicates.

Comparison of gene expression changes across different datasets. Unless stated otherwise, heatmaps of logFC were used for the comparison of gene expression changes across different datasets (scRNA-seq, FACS/bulk RNA-seq, FACS/qRT-PCR). Heatmaps are much more informative than Venn diagrams as they display gene identity and the degree of expression change. Our independent datasets were in a very good agreement with each other, as only a few inconsistencies in the expression changes of certain individual genes were observed. These changes more likely reflect slight differences in the cell populations identified either informatically (for scRNA-seq) or by antibody labeling (for FACS/bulk RNA-seq). For example, in our flow cytometry experiments we used anti-ACSA-2 to isolate and purify ASC^{93,94}, but a recent study showed that this marker is not expressed at the same level by all ASC⁹⁵. Thus, this marker may slightly enrich some subpopulations of ASC more than others. Of note, the existence of diverse subpopulations of ASC with distinct region-specific transcriptomic signatures has been recently demonstrated¹² and verified by our scRNA-seq analysis (see Supplementary Fig. 8), while aging-associated gene expression changes in different regional ASCs have been also documented^{7,96,97}. Therefore, it is possible that informatics-based identification, and FACS-based isolation/purification, define cell populations that are very similar, but not identical, to each other, potentially contributing to discrepancies when comparative analyses are used.

RNAscope in situ hybridization. RNAscope fluorescent in situ hybridization was performed on fresh-frozen brain tissue from 16 mice (8 young and 8 old). For sample preparation, mice were CO₂ anesthetized, and brains were rapidly extracted and embedded in OCT (Tissue Tek) on dry ice, and then stored at –80°C until further processing. We collected 14-µm cryostat sections and RNAscope hybridizations were carried out according to the manufacturer's instructions, using the RNAscope Multiplex Fluorescent Manual Assay kit (Advanced Cell Diagnostics). Briefly, thawed sections were dehydrated in sequential incubations with ethanol, followed by 30-min Protease IV treatment and washing in 1× PBS. Appropriate combinations of hybridization probes were incubated for 2 h at 40°C, followed by four amplification steps, 4,6-diamidino-2-phenylindole (DAPI) counterstaining, and mounting with Prolong Gold mounting medium (Thermo Fisher Scientific no. P36930). Brain regions were selected considering the high expression levels of the examined genes, according to the Allen Brain Atlas⁹⁸. For single-probe analysis, probes against *Rpl6* (ACD no. 300031), *Malat1* (ACD

no. 313391) and *Meg3* (ACD no. 527201) were tested and labeled with the fluorophore Atto-550 nm. For each mouse, 3–4 bregma-matched sections were imaged. Images (4 per brain section) were acquired with a Zeiss LSM 880 Confocal Microscope with identical settings across young and old sections and represented as maximum intensity projections of acquired confocal z stacks. Analysis was done with the CellProfiler software (v.3)³⁹ with the following specifications for different target probes: *Malat1/Meg3*: only puncta with a diameter between 4 and 8 pixels that were located within the nuclei were quantified; *Rpl6*: only puncta with a diameter between 4 and 8 pixels that were located within the perinuclear space (within 70 pixels of the DAPI-positive nuclei) were quantified. For dual-probe analysis, RNAscope was performed as described above, but here imaging settings were kept identical across all young and old brain sections and all probes tested. Probes against *Cd9* (ACD no. 430631), *Rps23* (ACD no. 571741), *Pdgfra* (ACD no. 480661-C3) and *Irgam* (ACD no. 311491-C3) were tested. Target probes (*Cd9*, *Rps23*) were labeled by fluorophore Atto-550nm, while cell-type markers (*Pdgfra*, *Irgam*) were labeled by fluorophore Alexa-488nm. An empty channel (Atto-647) was collected for every image processed to account for autofluorescence from lipofuscin granules largely associated in the aged brain with MG¹⁰⁰. In our imaging we observed that lipofuscin autofluorescence mainly interfered with Alexa-488 channel. Imaging analysis was performed as above with the following specifications for target probes (*Cd9*, *Rps23*): only puncta with a diameter between 6 and 15 pixels that were located within an OPC's or MG's perinuclear space (within 70 pixels of the DAPI-positive nuclei) were quantified. OPC and MG were defined as cells that contained at least two *Pdgfra*⁺ or *Irgam*⁺ puncta, respectively (diameter 6–15 pixels). It is important to note that due to the high degree of homology among ribosomal protein genes, certain pseudogenes and predicted mouse genes, probes designed against *Rpl6* and *Rps23*, may also cross-detect off-targets, based on the specificity criteria provided by the vendor: the *Rpl6* probe may cross-detect *Gm13397* and *Gm6807*; the *Rps23* probe may cross-detect *Gm8624*, *Gm3189*, *Gm10689*, *Rps23-ps1* and *Rps23-ps2*.

Immunohistochemistry. For immunohistochemistry experiments, 14 mouse brains (7 young and 7 old) were processed. For preparation of free-floating tissue sections, mice were perfused intracardially with 1× PBS followed by 4% paraformaldehyde; brains were removed and embedded in 3% agarose, and serial 30-µm-thick coronal sections were cut in a vibrating microtome and were kept in 1× PBS with 0.1% sodium azide at 4°C until staining. For preparation of fresh-frozen tissue sections (used only to show the co-expression of IL33 and OLIG2), mice were CO₂ anesthetized, brains were rapidly extracted and embedded in OCT, and serial 14-µm-thick coronal sections were cut in a cryostat and then fixed in 4% paraformaldehyde before staining. Immunostaining was performed with standard procedures. Briefly, sections were washed thoroughly in 1× PBS and incubated in a permeabilization/blocking solution (10% normal goat serum (or 10% donkey serum, or 2% horse serum), 0.25% Triton X-100, 1× PBS) for 1 h at room temperature. Sections were then incubated overnight at 4°C with the following primary antibodies in blocking solution (typically at 1:100 dilution): goat polyclonal anti-SPARC (R&D Systems no. AF942), rabbit polyclonal anti-IBA1 (Wako no. 019-19741), goat polyclonal anti-IL33 (R&D Systems no. AF3626) and mouse monoclonal anti-OLIG2 (Millipore no. MABN50). Alexa Fluor secondary antibodies (Invitrogen) were used for detection of primary antibodies in 1% normal goat (or donkey serum or horse serum), 1× PBS for 1–2 h at room temperature. Hoechst 33342 was used to label nuclei. Imaging was performed with a Zeiss ELYRA super-resolution confocal microscope (free-floating tissue sections) or a Zeiss LSM 880 confocal microscope (fresh-frozen tissue sections) at ×20 and ×40 magnifications. Images were visualized with Zeiss Zen software (blue edition; v.2.6). For each mouse, 3–4 bregma-matched sections were imaged. Images were represented as maximum intensity projections of acquired confocal z stacks. Analysis was done with Image J software (v.1.49).

Statistics and reproducibility. No statistical methods were used to predetermine sample sizes; our sample sizes were determined iteratively. No randomization was performed. Data collection and analysis were not performed blind to the conditions of the experiments. All statistical analyses were performed with R (v.3.3.4) or GraphPad Prism (v.7.04). Unless otherwise stated, to generate *P* values for cell counts and other metrics/variables, we used the Mann–Whitney *U*-test¹⁰¹. All *P* values were modified to a FDR of 5% with the Benjamin–Hochberg procedure¹⁰². For validation of gene expression changes by qRT-PCR, immunohistochemistry, and RNAscope in situ hybridization assays, data distribution was assumed to be normal for each analysis, but this was not formally tested.

Reporting Summary. Further information on research design is available in the Nature Research Reporting Summary linked to this article.

Data availability

The raw single-cell RNA sequencing data are available through NCBI's Gene Expression Omnibus (GEO) under the accession number [GSE129788](https://www.ncbi.nlm.nih.gov/geo/query/acc.cgi?acc=GSE129788). The processed datasets can be readily viewed, explored and downloaded through our web-based interactive viewers at https://portals.broadinstitute.org/single_cell/study/aging-mouse-brain and <http://shiny.baderlab.org/AgingMouseBrain/>.

Code availability

The code used to perform analysis of the sequencing data was an adaptation of standard R packages, such as Seurat and MAST, as described in the Methods section. The code used for the ligand–receptor interaction analyses is available on GitHub at <https://github.com/BaderLab/AgingMouseBrainCCInx>. More detailed information is available upon request.

References

- Zhang, R., Lahens, N. F., Ballance, H. I., Hughes, M. E. & Hogenesch, J. B. A circadian gene expression atlas in mammals: implications for biology and medicine. *Proc. Natl Acad. Sci. USA* **111**, 16219–16224 (2014).
- Saxena, A. et al. Trehalose-enhanced isolation of neuronal sub-types from adult mouse brain. *Biotechniques* **52**, 381–385 (2012).
- Zheng, G. X. et al. Massively parallel digital transcriptional profiling of single cells. *Nat. Commun.* **8**, 14049 (2017).
- Satija, R., Farrell, J. A., Gennert, D., Schier, A. F. & Regev, A. Spatial reconstruction of single-cell gene expression data. *Nat. Biotechnol.* **33**, 495–502 (2015).
- Macosko, E. Z. et al. Highly parallel genome-wide expression profiling of individual cells using nanoliter droplets. *Cell* **161**, 1202–1214 (2015).
- Butler, A., Hoffman, P., Smibert, P., Papalexi, E. & Satija, R. Integrating single-cell transcriptomic data across different conditions, technologies, and species. *Nat. Biotechnol.* **36**, 411–421 (2018).
- Marques, S. et al. Oligodendrocyte heterogeneity in the mouse juvenile and adult central nervous system. *Science* **352**, 1326–1329 (2016).
- Ubink, R. & Hokfelt, T. Expression of neuropeptide Y in olfactory ensheathing cells during prenatal development. *J. Comp. Neurol.* **423**, 13–25 (2000).
- Beckervordersandforth, R. et al. In vivo fate mapping and expression analysis reveals molecular hallmarks of prospectively isolated adult neural stem cells. *Cell Stem Cell* **7**, 744–758 (2010).
- Codega, P. et al. Prospective identification and purification of quiescent adult neural stem cells from their in vivo niche. *Neuron* **82**, 545–559 (2014).
- Llorens-Bobadilla, E. et al. Single-cell transcriptomics reveals a population of dormant neural stem cells that become activated upon brain injury. *Cell Stem Cell* **17**, 329–340 (2015).
- Shah, P. T. et al. Single-cell transcriptomics and fate mapping of ependymal cells reveals an absence of neural stem cell function. *Cell* **173**, 1045–1057. e1049 (2018).
- Zywitzka, V., Misios, A., Bunatyan, L., Willnow, T. E. & Rajewsky, N. Single-cell transcriptomics characterizes cell types in the subventricular zone and uncovers molecular defects impairing adult. *Neurogenesis. Cell Rep.* **25**, 2457–2469. e2458 (2018).
- Liu, Y. et al. CD44 expression identifies astrocyte-restricted precursor cells. *Dev. Biol.* **276**, 31–46 (2004).
- Hochgerner, H., Zeisel, A., Lonnerberg, P. & Linnarsson, S. Conserved properties of dentate gyrus neurogenesis across postnatal development revealed by single-cell RNA sequencing. *Nat. Neurosci.* **21**, 290–299 (2018).
- Tasic, B. et al. Adult mouse cortical cell taxonomy revealed by single cell transcriptomics. *Nat. Neurosci.* **19**, 335–346 (2016).
- Zhang, X. et al. BAIAP3, a C2 domain-containing Munc13 protein, controls the fate of dense-core vesicles in neuroendocrine cells. *J. Cell Biol.* **216**, 2151–2166 (2017).
- Zeisel, A. et al. Brain structure. Cell types in the mouse cortex and hippocampus revealed by single-cell RNA-seq. *Science* **347**, 1138–1142 (2015).
- Vanlandewijck, M. et al. A molecular atlas of cell types and zonation in the brain vasculature. *Nature* **554**, 475–480 (2018).
- Straub, A. C. et al. Endothelial cell expression of haemoglobin alpha regulates nitric oxide signalling. *Nature* **491**, 473–477 (2012).
- Han, X. et al. Mapping the mouse cell atlas by Microwell-Seq. *Cell* **172**, 1091–1107. e1017 (2018).
- Geijtenbeek, T. B. et al. Identification of DC-SIGN, a novel dendritic cell-specific ICAM-3 receptor that supports primary immune responses. *Cell* **100**, 575–585 (2000).
- Artegiani, B. et al. A single-cell RNA sequencing study reveals cellular and molecular dynamics of the hippocampal neurogenic niche. *Cell Rep.* **21**, 3271–3284 (2017).
- Romanov, R. A. et al. Molecular interrogation of hypothalamic organization reveals distinct dopamine neuronal subtypes. *Nat. Neurosci.* **20**, 176–188 (2017).
- Tepe, B. et al. Single-cell RNA-Seq of mouse olfactory bulb reveals cellular heterogeneity and activity-dependent molecular census of adult-born neurons. *Cell Rep.* **25**, 2689–2703. e2683 (2018).
- Mrdjen, D. et al. High-dimensional single-cell mapping of central nervous system immune cells reveals distinct myeloid subsets in health, aging, and disease. *Immunity* **48**, 380–395. e386 (2018).

77. Finak, G. et al. MAST: a flexible statistical framework for assessing transcriptional changes and characterizing heterogeneity in single-cell RNA sequencing data. *Genome Biol.* **16**, 278 (2015).
78. Reimand, J. et al. Pathway enrichment analysis and visualization of omics data using g:Profiler, GSEA, Cytoscape and EnrichmentMap. *Nat. Protoc.* **14**, 482–517 (2019).
79. Kucera, M., Isserlin, R., Arkhangorodsky, A. & Bader, G. D. AutoAnnotate: a Cytoscape app for summarizing networks with semantic annotations. *F1000Research* **5**, 1717 (2016).
80. Kirouac, D. C. et al. Dynamic interaction networks in a hierarchically organized tissue. *Mol. Syst. Biol.* **6**, 417 (2010).
81. Uhlen, M. et al. Proteomics. Tissue-based map of the human proteome. *Science* **347**, 1260419 (2015).
82. Razick, S., Magklaras, G. & Donaldson, I. M. iRefIndex: a consolidated protein interaction database with provenance. *BMC Bioinforma.* **9**, 405 (2008).
83. Cerami, E. G. et al. Pathway Commons, a web resource for biological pathway data. *Nucleic Acids Res.* **39**, D685–D690 (2011).
84. Stark, C. et al. BioGRID: a general repository for interaction datasets. *Nucleic Acids Res.* **34**, D535–D539 (2006).
85. Soumillon, M., Cacchiarelli, D., Semrau, S., van Oudenaarden, A. & Mikkelsen, T. S. Characterization of directed differentiation by high-throughput single-cell RNA-seq. Preprint at *bioRxiv* <https://www.biorxiv.org/content/10.1101/003236v1> (2014).
86. Derr, A. et al. End Sequence Analysis Toolkit (ESAT) expands the extractable information from single-cell RNA-seq data. *Genome Res.* **26**, 1397–1410 (2016).
87. Dobin, A. et al. STAR: ultrafast universal RNA-seq aligner. *Bioinformatics* **29**, 15–21 (2013).
88. Li, H. et al. The Sequence Alignment/Map format and SAMtools. *Bioinformatics* **25**, 2078–2079 (2009).
89. Anders, S. & Huber, W. Differential expression analysis for sequence count data. *Genome Biol.* **11**, R106 (2010).
90. Love, M. I., Huber, W. & Anders, S. Moderated estimation of fold change and dispersion for RNA-seq data with DESeq2. *Genome Biol.* **15**, 550 (2014).
91. Livak, K. J. & Schmittgen, T. D. Analysis of relative gene expression data using real-time quantitative PCR and the 2(-Delta Delta C(T)) Method. *Methods* **25**, 402–408 (2001).
92. Eisenberg, E. & Levanon, E. Y. Human housekeeping genes, revisited. *Trends Genet.* **29**, 569–574 (2013).
93. Sharma, K. et al. Cell type- and brain region-resolved mouse brain proteome. *Nat. Neurosci.* **18**, 1819–1831 (2015).
94. Tabula Muris, C. et al. Single-cell transcriptomics of 20 mouse organs creates a Tabula Muris. *Nature* **562**, 367–372 (2018).
95. Kantzer, C. G. et al. Anti-ACSA-2 defines a novel monoclonal antibody for prospective isolation of living neonatal and adult astrocytes. *Glia* **65**, 990–1004 (2017).
96. Boisvert, M. M., Erikson, G. A., Shokhiev, M. N. & Allen, N. J. The aging astrocyte transcriptome from multiple regions of the mouse brain. *Cell Rep.* **22**, 269–285 (2018).
97. Soreq, L. et al. Major shifts in glial regional identity are a transcriptional hallmark of human brain. *Aging Cell Rep.* **18**, 557–570 (2017).
98. Lein, E. S. et al. Genome-wide atlas of gene expression in the adult mouse brain. *Nature* **445**, 168–176 (2007).
99. Carpenter, A. E. et al. CellProfiler: image analysis software for identifying and quantifying cell phenotypes. *Genome Biol.* **7**, R100 (2006).
100. Xu, H., Chen, M., Manivannan, A., Lois, N. & Forrester, J. V. Age-dependent accumulation of lipofuscin in perivascular and subretinal microglia in experimental mice. *Aging Cell* **7**, 58–68 (2008).
101. Mann, H. B. & Whitney, D. R. On a test of whether one of two random variables is stochastically larger than the other. *Ann. Math. Stat.* **18**, 50–60 (1947).
102. Benjamini, Y. & Hochberg, Y. Controlling the false discovery rate: a practical and powerful approach to multiple testing. *J. R. Stat. Soc. Ser. B* **57**, 289–300 (1995).

Reporting Summary

Nature Research wishes to improve the reproducibility of the work that we publish. This form provides structure for consistency and transparency in reporting. For further information on Nature Research policies, see [Authors & Referees](#) and the [Editorial Policy Checklist](#).

Statistics

For all statistical analyses, confirm that the following items are present in the figure legend, table legend, main text, or Methods section.

n/a Confirmed

- The exact sample size (n) for each experimental group/condition, given as a discrete number and unit of measurement
- A statement on whether measurements were taken from distinct samples or whether the same sample was measured repeatedly
- The statistical test(s) used AND whether they are one- or two-sided
Only common tests should be described solely by name; describe more complex techniques in the Methods section.
- A description of all covariates tested
- A description of any assumptions or corrections, such as tests of normality and adjustment for multiple comparisons
- A full description of the statistical parameters including central tendency (e.g. means) or other basic estimates (e.g. regression coefficient) AND variation (e.g. standard deviation) or associated estimates of uncertainty (e.g. confidence intervals)
- For null hypothesis testing, the test statistic (e.g. F , t , r) with confidence intervals, effect sizes, degrees of freedom and P value noted
Give P values as exact values whenever suitable.
- For Bayesian analysis, information on the choice of priors and Markov chain Monte Carlo settings
- For hierarchical and complex designs, identification of the appropriate level for tests and full reporting of outcomes
- Estimates of effect sizes (e.g. Cohen's d , Pearson's r), indicating how they were calculated

Our web collection on [statistics for biologists](#) contains articles on many of the points above.

Software and code

Policy information about [availability of computer code](#)

Data collection

Single-cell RNA-seq data were acquired using the Cell Ranger software (version 1.2).
RNAscope ISH and IHC images were acquired using the Zeiss Zen image software (version 2.6).
qRT-PCR data were acquired using QuantStudio 12K FLlex Real-Time PCR software (version 1.2.2).

Data analysis

Single-cell RNA-seq data were analyzed in R Studio (version 3.3.4) using the packages Seurat (version 2.3) and MAST (version 1.6.1).
Bulk RNA-seq data were analyzed in R Studio (version 3.2.3) using the package DESeq2 (version 3.7).
Processed single cell RNA-seq datasets were analyzed in GSEA software (version 3.0) and in Cytoscape software (version 3.5.1) using the AutoAnnotate app (version 1.2) and the EnrichmentMap app (version 3.0.)
RNAscope ISH images were analyzed in CellProfiler software (version 3).
IHC images were analyzed in Image J software (version 1.49).
FACS data were analyzed in FlowJo software (version 10).
qRT-PCR data were analyzed in GraphPad Prism software (version 7.04).

The code used for the ligand-receptor interaction analyses is available on GitHub at:
<https://github.com/BaderLab/AgingMouseBrainCClnx>

For manuscripts utilizing custom algorithms or software that are central to the research but not yet described in published literature, software must be made available to editors/reviewers. We strongly encourage code deposition in a community repository (e.g. GitHub). See the Nature Research [guidelines for submitting code & software](#) for further information.

Data

Policy information about [availability of data](#)

All manuscripts must include a [data availability statement](#). This statement should provide the following information, where applicable:

- Accession codes, unique identifiers, or web links for publicly available datasets
- A list of figures that have associated raw data
- A description of any restrictions on data availability

The raw sequencing data are available through NCBI's Gene Expression Omnibus (GEO) under the accession number: GSE129788.

The processed datasets can be viewed, explored and downloaded through the Broad's Single Cell Data Portal at:

https://portals.broadinstitute.org/single_cell/study/aging-mouse-brain

The intercellular communication network is available for exploration and download at:

<http://shiny.baderlab.org/AgingMouseBrain/>

Field-specific reporting

Please select the one below that is the best fit for your research. If you are not sure, read the appropriate sections before making your selection.

- Life sciences Behavioural & social sciences Ecological, evolutionary & environmental sciences

For a reference copy of the document with all sections, see [nature.com/documents/nr-reporting-summary-flat.pdf](https://www.nature.com/documents/nr-reporting-summary-flat.pdf)

Life sciences study design

All studies must disclose on these points even when the disclosure is negative.

Sample size	Samples sizes for each experiment are clearly delineated in the manuscript. No statistical methods were used to predetermine sample sizes; our sample sizes were determined iteratively. For the single cell RNA-seq the total number of young and old animals, as well as, the number of single cells analyzed was set to ensure that multiple animals contributed to each reported cell population and to allow the comparison of young and old cell types. Same rationale was followed for all the validation experiments.
Data exclusions	All exclusion criteria are established during exploratory data analysis and are delineated in the relevant sections of the Methods. In brief, for scRNA-seq experiments, data from poor quality cells and outliers (having greater than 30% mitochondrial RNA, less than 200 UMIs, less than 250 nGenes, greater than 30,000 UMIs, greater than 6,000 nGenes), from good quality cells (derived from less than half of the young and old animals), and from doublets/multiplets were excluded from the analysis. For qRT-PCR experiments, samples with Vcp Ct values greater than 29 were excluded from the analysis. For FISH and IHC experiments, no images were excluded.
Replication	Findings that are highlighted in the manuscript were successfully reproduced using independent methodologies (FACS/bulk RNA-seq, FACS/qRT-PCR, RNAscope ISH, and IHC).
Randomization	No randomization was used as there was no treatment in our study. However, young and old mice were randomly assigned to the different sets of experiments (single cell RNA-seq, FACS/bulk RNA-seq, FACS/qRT-PCR, RNAscope ISH, and IHC).
Blinding	Blinding was not possible, as knowledge of the experimental conditions was required during the data collection and analyses.

Reporting for specific materials, systems and methods

We require information from authors about some types of materials, experimental systems and methods used in many studies. Here, indicate whether each material, system or method listed is relevant to your study. If you are not sure if a list item applies to your research, read the appropriate section before selecting a response.

Materials & experimental systems

n/a	Involved in the study
<input type="checkbox"/>	<input checked="" type="checkbox"/> Antibodies
<input checked="" type="checkbox"/>	<input type="checkbox"/> Eukaryotic cell lines
<input checked="" type="checkbox"/>	<input type="checkbox"/> Palaeontology
<input type="checkbox"/>	<input checked="" type="checkbox"/> Animals and other organisms
<input checked="" type="checkbox"/>	<input type="checkbox"/> Human research participants
<input checked="" type="checkbox"/>	<input type="checkbox"/> Clinical data

Methods

n/a	Involved in the study
<input checked="" type="checkbox"/>	<input type="checkbox"/> ChIP-seq
<input type="checkbox"/>	<input checked="" type="checkbox"/> Flow cytometry
<input checked="" type="checkbox"/>	<input type="checkbox"/> MRI-based neuroimaging

For FACS (all the following antibodies used at a final concentration 3µg/ml):

APC anti-ACSA-2 (Miltenyi Biotec #130-102-315)

<https://www.miltenyibiotec.com/US-en/products/mac-flow-cytometry/antibodies/primary-antibodies/anti-acsa-2-antibodies-mouse-ih3-18a3-1-10.html>

BV786 anti-CD31 (BD Biosciences #740870)

<http://www.bdbiosciences.com/us/reagents/research/antibodies-buffers/immunology-reagents/anti-mouse-antibodies/cell-surface-antigens/bv786-rat-anti-mouse-cd31-mec-133/p/740870>

BV786 anti-CD31 (BD Biosciences #740879)

<https://www.bdbiosciences.com/us/reagents/research/antibodies-buffers/immunology-reagents/anti-mouse-antibodies/cell-surface-antigens/bv786-rat-anti-mouse-cd31-390/p/740879>

BV510 anti-CD11b (BD Biosciences #562950)

<https://www.bdbiosciences.com/eu/applications/research/stem-cell-research/mesenchymal-stem-cell-markers-bone-marrow/mouse/negative-markers/bv510-rat-anti-cd11b-m170/p/562950>

PE anti-CD200 (BioLegend #123808)

<https://www.biolegend.com/en-us/products/pe-anti-mouse-cd200-ox2-antibody-4424>

Alexa Fluor 488 anti-O4 (R&D Systems #FAB1326G)

https://www.rndsystems.com/products/oligodendrocyte-marker-o4-alex-fluor-488-conjugated-antibody-o4_fab1326g

BV605 anti-CD140a (BD Biosciences #740380)

<https://www.bdbiosciences.com/us/reagents/research/antibodies-buffers/immunology-reagents/anti-mouse-antibodies/cell-surface-antigens/bv605-rat-anti-mouse-cd140a-apa5/p/740380>

APC anti-CD133 (Miltenyi Biotec #130-102-197)

<https://www.miltenyibiotec.com/US-en/products/mac-flow-cytometry/antibodies/primary-antibodies/anti-prominin-1-antibodies-mouse-mb9-3g8-1-10.html#apc:30-ug-in-1-ml>

APC anti-CD133 (eBioscience #17-1331-81)

<https://www.thermofisher.com/antibody/product/CD133-Prominin-1-Antibody-clone-13A4-Monoclonal/17-1331-81>

PE anti-CD24a (BD Biosciences #553262)

<http://www.bdbiosciences.com/us/applications/research/stem-cell-research/cancer-research/mouse/pe-rat-anti-mouse-cd24-m169/p/553262>

PE anti-CD24a (BioLegend #138504)

<https://www.biolegend.com/en-us/products/pe-anti-mouse-cd24-antibody-6617>

For IHC (all primary antibodies used at 1:100 dilution):

anti-SPARC (R&D Systems #AF942)

https://www.rndsystems.com/products/mouse-sparc-antibody_af942

anti-IBA1 (Wako #019-19741)

<https://labchem-wako.fujifilm.com/us/category/01213.html>

anti-IL33 (R&D Systems#AF3626)

https://www.rndsystems.com/products/mouse-il-33-antibody_af3626

anti-OLIG2 (Millipore #MABN50)

http://www.emdmillipore.com/US/en/product/Anti-Olig2-Antibody-clone-211F1.1,MM_NF-MABN50

For IHC (all secondary antibodies used at 1:250 dilution):

anti-rabbit-Alexa Fluor 488 (Invitrogen #A21206)

<https://www.thermofisher.com/antibody/product/Donkey-anti-Rabbit-IgG-H-L-Highly-Cross-Adsorbed-Secondary-Antibody-Polyclonal/A-21206>

anti-mouse-Alexa Fluor 546 (Invitrogen #A10036)

<https://www.thermofisher.com/antibody/product/Donkey-anti-Mouse-IgG-H-L-Highly-Cross-Adsorbed-Secondary-Antibody-Polyclonal/A10036>

anti-goat-Alexa Fluor 488 (Invitrogen #A11055)

<https://www.thermofisher.com/antibody/product/Donkey-anti-Goat-IgG-H-L-Cross-Adsorbed-Secondary-Antibody-Polyclonal/A-11055>

anti-goat-Alexa Fluor 546 (Invitrogen #A11056)

<https://www.thermofisher.com/antibody/product/Donkey-anti-Goat-IgG-H-L-Cross-Adsorbed-Secondary-Antibody-Polyclonal/A-11056>

Validation

All the above are well characterized commercial antibodies. For each one, the specificity has been tested by the manufacturer and verified independently by previous published studies. Validation profiles and relevant citations can be found in the links provided.

Animals and other organisms

Policy information about [studies involving animals](#); [ARRIVE guidelines](#) recommended for reporting animal research

Laboratory animals

For all the experiments, only male C57BL/6J mice (JAX #000664) were used. Young mice were at 2-3 months of age, and old male mice at 21-22 months of age.

Wild animals

This study did not contain wild animals.

Field-collected samples

This study did not contain field-collected samples.

Ethics oversight

All experimental procedures were approved in advance by the Animal Care and Use Committee of Harvard University (AEP #10-23) and are in compliance with federal and state laws.

Note that full information on the approval of the study protocol must also be provided in the manuscript.

Flow Cytometry

Plots

Confirm that:

- The axis labels state the marker and fluorochrome used (e.g. CD4-FITC).
- The axis scales are clearly visible. Include numbers along axes only for bottom left plot of group (a 'group' is an analysis of identical markers).
- All plots are contour plots with outliers or pseudocolor plots.
- A numerical value for number of cells or percentage (with statistics) is provided.

Methodology

Sample preparation

For the flow cytometry experiments, we used single cell suspensions derived from either young or old mouse brains.

Instrument

Moflo Astrios instrument (Beckman Coulter).

Software

Data were analyzed using the FlowJo software (version 10).

Cell population abundance

ACSA-2+ astrocytes: 500,000 cells/brain
 CD11b+ microglia: 130,000 cells/brain
 CD31+ endothelial cells: 30,000 cells/brain
 CD24a+/CD133+ ependymocytes: 30,000 cells/brain

Gating strategy

Gates were set manually by using compensation beads (Life Technologies #A10497) and appropriate control samples.

- Tick this box to confirm that a figure exemplifying the gating strategy is provided in the Supplementary Information.